Three-flavor oscillation solutions for the solar neutrino problem

H. Schlattl*
Max-Planck-Institut für Astrophysik, Karl-Schwarzschild-Str. 1, 85741 Garching, Germany
(Received 5 May 2000; revised manuscript received 6 February 2001; published 1 June 2001)

The good agreement of standard solar models with helioseismology and the combined analysis of the solar neutrino experiments suggest that the solution of the solar neutrino problem is located in particle physics rather than in astrophysics. The most promising solution is neutrino oscillations, which usually are analyzed within the reduced two-flavor scheme, because the solutions found therein reasonably well reproduce the recent data of Super-Kamiokande about the recoil-electron energy spectrum, zenith-angle and seasonal variations, and the event rate data of all the neutrino detectors. In this work, however, a survey of the complete parameter space of three-flavor oscillations is performed. Basically 8 three-flavor solutions could be identified, where the best one with $\Delta m^2_{12}=2.7\times10^{-10}$ eV^2, $\Delta m^2_{13}=1.0\times10^{-5}$ eV^2, $\Theta_{12}=23°$, and $\Theta_{13}=1.3°$ (denoted SVO) is slightly more probable than any two-flavor solution. However, as the greatest value for Δm^2_{23} of these three-flavor solutions is about 2.5×10^{-4} eV^2, none of these solutions is consistent with the results of the atmospheric neutrino problem where $\Delta m^2_{23}\gtrsim10^{-3}$ eV^2. The relatively weak improvement of the fit using three-flavor instead of two-flavor oscillations, which appears to be due to an inconsistency of the different kinds of data, indicates that there are possibly still systematic errors in at least one data set or that the statistics is not yet sufficient. In addition, the abilities of SNO and Borexino to discriminate the various two- and three-flavor solutions are investigated. Only with very good statistics in these experiments can the correct solution to the solar neutrino problem be identified unambiguously.

DOI: 10.1103/PhysRevD.64.013009 PACS number(s): 14.60.Pq, 26.65.+t, 96.60.Jw

I. INTRODUCTION

From the beginning of the first measurements of the solar neutrino flux on Earth [1] until the present time, the origin of the solar neutrino problem has not yet be resolved totally. While previously inaccurate or unknown physics used in solar-model calculations could have been made responsible for the discrepancy between measured and predicted solar neutrino flux, this kind of solution can presently almost be ruled out, basically for two reasons.

First, the high precision in the measurements of the solar *p*-mode frequencies and the development of helioseismological inversion techniques enable the determination of the solar sound-speed profile with high accuracy [2]. Comparison with standard solar models containing improved input physics such as opacity, equation of state, and microscopic diffusion shows excellent agreement with seismic models [3–5]. Predictions for the event rates in the solar neutrino detectors deduced from these standard solar models still are inconsistent with the measurements, confirming the solar neutrino problem (Table II).

Second, the three types of currently operating experiments, the chlorine detector [1], the gallium experiments GALLEX/GNO [6] and SAGE [7], and the Čerenkov-light counter Super-Kamiokande have different neutrino-energy thresholds. This allows to determine the contribution of different parts of the solar neutrino spectrum to the total flux without explicitly taking into account solar-model calculations. From this analysis it has been inferred that the experimental results can be explained only with huge changes in the nuclear fusion rates. The best fit with the data is obtained even with a *negative* flux of neutrinos created in the electron-capture process of ^{7}Be [8]. Nevertheless, strong modifications of the reaction cross sections would be difficult to explain experimentally and theoretically. Moreover, even if a presently unknown physical process could account for the demanded changes, the resulting solar models would hardly be consistent with helioseismology [9].

The most promising approach to the solution of the solar neutrino problem is an extension to the particle-physics standard model—neutrino mixing. Analogous to Cabibbo-Kobayashi-Maskawa (CKM) mixing in the quark sector, weak and mass eigenstates of neutrinos are supposed not to be identical but connected by a unitary transformation.

Under this assumption an initial solar electron neutrino can be converted during its propagation to the Earth into another flavor, a μ or τ neutrino (*just-so* oscillations [10]). Furthermore, the neutrinos may coherently scatter forward in solar matter [Mikheyev-Smirnov-Wolfenstein (MSW) effect [11]], altering the conversion probability for a certain set of mixing parameters.

The possible values for the mixing parameters, with which the measured event rates in all detectors can be reproduced simultaneously, have been derived by various authors [12,13], but oscillations between only two flavors usually are taken into account.

Recently Super-Kamiokande has published more detailed information about the energy distribution of the recoiled electrons and the zenith-angle dependence of the neutrino signal [14,15]. In the analysis of the 825-day data it became clear that it is not possible to explain satisfactorily these data *and* the event rates of all detectors by one set of mixing parameters (see [16]): An excess of event rates in the high-energy bins was inconsistent with the other data.

It was the initial motivation of the present work to examine whether an expansion of the neutrino analysis to the more general three-flavor case could resolve this discrepancy

*Email address: schlattl@mpa-garching.mpg.de

between the different types of data. However, after the Super-Kamiokande group reanalyzed their data and included new data (1117 days in total), the excess in the energy-bin data diminished and now all data can be explained simultaneously by two-flavor oscillations. Furthermore, the ^{8}B-neutrino spectrum has been redetermined by performing new measurements of the electron spectrum of the ^{8}B decay [17] (hereafter OG00). Although within the error ranges the spectrum is in agreement with the one of Ref. [18] (hereafter BL96), the number of high-energetic neutrinos is overall higher than previously thought. Thus, the excess in high-energy bins is further reduced which yields a yet slightly better reproduction of the data by two-flavor solutions (see Sec. IV A). After the analyses performed in this work were finished, new calculations of the cross section of the ^{3}He proton capture, which produces the most energetic *hep*-neutrinos, have been published yielding a 4.5 times higher value than previously evaluated [19]. Since these neutrinos were contributing about 1% to the number of events in the highest energy bin of Super-Kamiokande, using the new $^3\mathrm{He}+p$ cross section increases the expected rates in this energy bin by about 4%. This probably leads to a slightly improved fit of the two-flavor solutions to the data. However, as mainly the highest energy bin is influenced and the difference including the new instead of the old $^3\mathrm{He}+p$ cross section is small, no significant impact on the results of this work is expected, where still the smaller $^3\mathrm{He}+p$ cross section of Ref. [20] has been used. Anyway, it is presently still not clear which solution to the solar neutrino problem is the correct one, and hence all possible solutions should be deduced.

Therefore, in this work the most general case of three-flavor oscillations is investigated without making any assumptions about the mass scale as, for instance, inspired by the atmospheric neutrino problem. The latter is taken in various publications [21–24] as a constraint to investigate three-flavor oscillations. Here, the aim is to examine whether the expansion to three flavors leads to new solutions with which the fits to all kinds of data can be improved compared to the usual two-flavor analysis. The implications for the atmospheric neutrino puzzle are discussed afterwards.

In Sec. II the equations for three-flavor oscillations are derived from the solution to the Klein-Gordon equation and the size of the parameter space is deduced. After describing the underlying solar model and the neutrino analysis in Sec. III, the results for two-flavor and three-flavor oscillations are shown (Sec. IV). Finally the abilities of forthcoming experiments like SNO and Borexino to discriminate the various solutions are discussed (Sec. V).

II. THEORY OF NEUTRINO OSCILLATIONS

In the following an overview of the basic equations for neutrino oscillations is provided with particular emphasis on the three-flavor case. A more thorough description can be found, e.g., in [25] or [9].

A. Vacuum oscillations

If neutrinos have mass, a mixing matrix similar to the Kobayashi-Maskawa matrix in the quark sector can be developed:

$$|\nu_\alpha\rangle = \begin{pmatrix} \nu_e \\ \nu_\mu \\ \nu_\tau \end{pmatrix} = \mathcal{U} \begin{pmatrix} \nu_1 \\ \nu_2 \\ \nu_3 \end{pmatrix} = \mathcal{U}|\nu_i\rangle, \tag{1}$$

where $|\nu_\alpha\rangle$ denotes the weak and $|\nu_i\rangle$ the mass eigenstates. The unitary matrix $\mathcal{U}$ can be parametrized by

$$\mathcal{U} = \begin{pmatrix} 1 & 0 & 0 \\ 0 & c_{23} & s_{23} \\ 0 & -s_{23} & c_{23} \end{pmatrix} \begin{pmatrix} c_{13} & 0 & s_{13}e^{-i\delta} \\ 0 & 1 & 0 \\ -s_{13}e^{i\delta} & 0 & c_{13} \end{pmatrix} \times \begin{pmatrix} c_{12} & s_{12} & 0 \\ -s_{12} & c_{12} & 0 \\ 0 & 0 & 1 \end{pmatrix}, \tag{2}$$

where s_{ij} and c_{ij} are abbreviations for $\sin\Theta_{ij}$ and $\cos\Theta_{ij}$ ($0 \leqslant \Theta_{ij} < \pi/2$), respectively, and δ is a CP-violating phase [26], which is neglected in the following.[1] The equation of motion for a neutrino beam in vacuum obeys the Klein-Gordon equation for free particles ($\hbar = c = 1$),

$$(\partial_t^2 - \nabla^2 + M^2)|\nu_i(t,\vec{r})\rangle = 0, \tag{3}$$

where the mass matrix M^2 is defined as

$$M^2 = \begin{pmatrix} m_1^2 & 0 & 0 \\ 0 & m_2^2 & 0 \\ 0 & 0 & m_3^2 \end{pmatrix},$$

with m_i being the mass of the neutrino mass eigenstate ν_i. Generally the solution is given by a superposition of plane waves $e^{i(\vec{k}\cdot\vec{r}-\omega t)}$ with the dispersion relation

$$\omega^2 = \vec{k}^2 + m^2.$$

In the case of the Sun with an almost stationary neutrino flux, $|\nu_i(t,\vec{r})\rangle$ can be expanded in components of fixed frequency $|\nu_i(\vec{r})\rangle_\omega e^{-i\omega t}$. For a spherically symmetric flux of relativistic neutrinos ($k \approx \omega$) one finally gets

$$-i\frac{\partial}{\partial r}|\nu_i(r)\rangle_\omega = \left(\omega - \frac{M^2}{2\omega}\right)|\nu_i(r)\rangle_\omega. \tag{4}$$

The constant ''potential'' ω can be removed by shifting the energy scale, and by using $t = r$, Eq. (4) can be formally written as a more familiar Schrödinger-type equation

$$i\frac{\partial}{\partial t}|\nu_i(t)\rangle_\omega = \mathcal{H}|\nu_i(t)\rangle_\omega, \tag{5}$$

[1]The effect of the CP-violating phase on the analysis of neutrino oscillation data has been elaborated on in [27].

with $\mathcal{H}=E_{\rm kin}\approx M^2/(2\omega)$. The general solution to this equation is

$$|\nu_i(t)\rangle_\omega = e^{-itM^2/(2\omega)}|\nu_i(t_0)\rangle_\omega. \tag{6}$$

The probability $P(r)_{\alpha\to\beta}$ to detect a neutrino ν_α with energy $E=\omega$ as a neutrino of type ν_β at distance $r=t$ from the source is therefore given by ($\mathcal{U}^{-1}=\mathcal{U}^\dagger$)

$$P(r)_{\alpha\to\beta}=|\langle\nu_\beta|\mathcal{U}e^{-ir(\Delta M^2/(2E))}\mathcal{U}^\dagger|\nu_\alpha\rangle|^2. \tag{7}$$

Using $\Delta m^2_{ij}=m^2_j-m^2_i$ the matrix ΔM^2 reads

$$\Delta M^2=M^2-m_1^2 Id_3=\begin{pmatrix}0&0&0\\0&\Delta m^2_{12}&0\\0&0&\Delta m^2_{13}\end{pmatrix}.$$

With the mass eigenstate of an electron neutrino being

$$\begin{pmatrix}\nu_1\\\nu_2\\\nu_3\end{pmatrix}_{\rm e}=\mathcal{U}^\dagger\begin{pmatrix}1\\0\\0\end{pmatrix}=\begin{pmatrix}c_{12}c_{13}\\s_{12}c_{13}\\s_{13}\end{pmatrix}, \tag{8}$$

Eq. (7) yields, for the survival probability of ν_e's in vacuum,

$$\begin{aligned}P(r)^{(3)}_{e\to e}=1&-\sin^2\left(\frac{\Delta m^2_{12}r}{4E}\right)\cos^4\Theta_{13}\sin^2 2\Theta_{12}\\&-\left[\sin^2\left(\frac{\Delta m^2_{13}r}{4E}\right)\cos^2\Theta_{12}\right.\\&\left.+\sin^2\left(\frac{\Delta m^2_{23}r}{4E}\right)\sin^2\Theta_{12}\right]\sin^2 2\Theta_{13}.\end{aligned} \tag{9}$$

The superscript (3) denotes the case of three-flavor mixing. $P^{(3)}_{e\to e}$ depends on four quantities, two mass-squared differences, Δm^2_{12} and Δm^2_{13} ($\Delta m^2_{23}=\Delta m^2_{13}-\Delta m^2_{12}$), and two mixing angles Θ_{12} and Θ_{13}. The third mixing angle Θ_{23} does not appear in Eq. (8) and hence $P^{(3)}_{e\to e}$ is independent of this quantity. The survival probabilities for ν_μ and ν_τ depend on Θ_{23}, but its value cannot be determined by solar-neutrino experiments, as in the energy range of solar neutrinos ν_μ and ν_τ interact equally with the detector material via neutral current (NC) interactions. Thus, only the total number of μ plus τ neutrinos, given by 1-$P^{(3)}_{e\to e}$, influences the event rates in detectors such as Super-Kamiokande, SNO, or Borexino.

For oscillations between two neutrino flavors where no mixing into the third flavor occurs (e.g., $\nu_e\leftrightarrow\nu_\mu$, $\Theta_{13}=0$), Eq. (9) simplifies to the well-known formula

$$P(r)^{(2)}_{e\to e}=1-\sin^2\left(\frac{\Delta m^2 r}{4E}\right)\sin^2 2\Theta, \tag{10}$$

where $\Delta m^2=\Delta m^2_{12}$ or Δm^2_{13} for ν_e-ν_μ and ν_e-ν_τ oscillations, respectively (Θ defined analogously).

B. Matter effect

During the propagation of neutrinos through the Sun they coherently scatter forward on the particles of the solar plasma. Unlike μ and τ neutrinos, which only interact via NC reactions, electron neutrinos can additionally couple via $\mathcal{W}$ bosons to electrons. Thus, the scattering cross section of a ν_e is altered in contrast to that of the other two neutrino flavors. This can lead to a resonant flavor transition, which may create a pure ν_μ or ν_τ beam from the originally created electron neutrinos, first theoretically postulated and described in [11] (MSW effect).

This effect can be included in Eq. (5) by substituting $\mathcal{H}$ with $\tilde{\mathcal{H}}=\mathcal{H}+V_{\rm eff}$, where

$$V_{\rm eff}=\sqrt{2}G_F N_e\mathcal{U}^\dagger\begin{pmatrix}1&0&0\\0&0&0\\0&0&0\end{pmatrix}\mathcal{U}$$

influences solely the ν_e contribution of the neutrino beam. G_F is the Fermi coupling constant and N_e the electron number density. The new Hamiltonian $\tilde{\mathcal{H}}$ is no longer diagonal in the mass basis. To evaluate the survival probability and thus $\exp(-i\tilde{\mathcal{H}}t)$ it is therefore necessary to diagonalize $\tilde{\mathcal{H}}$ by a unitary transformation $\mathcal{V}$:

$$\tilde{\mathcal{H}}_m=\begin{pmatrix}M_1&0&0\\0&M_2&0\\0&0&M_3\end{pmatrix}=\mathcal{V}^\dagger\tilde{\mathcal{H}}\mathcal{V}.$$

Similar to vacuum oscillations the constant phase $M_1 Id_3$ can be removed from $\tilde{\mathcal{H}}$ as it does not change the survival probability. The complicated analytical expressions for ΔM_{ij} have been evaluated in [28]. Recently, $\exp(-i\tilde{\mathcal{H}}t)$ has been calculated in [29] by using the Cayley-Hamilton theorem without explicitly deriving $\mathcal{V}$. In the present work, however, $\mathcal{V}$ and M_i are computed with a fast numerical algorithm using none of the analytic expressions.

C. Parameter space

Recently various publications appeared which dealt with the actual size of the necessary parameter space covering all possible solutions of the solar neutrino problem [30–32]. In this section the sometimes confusing statements about this topic are summarized and clarified.

The mixing angles can be defined to lie in the first quadrant by appropriately adjusting the neutrino field phases similar as in the quark sector [33]. This can also be verified from the final formulas, as, for instance, $P(r)^{(3)}_{e\to e}$ depends solely on the square of $\sin\Theta_{ij}$ and $\cos\Theta_{ij}$ ($ij=12,13$), respectively. Moreover, it has been shown in [30] that it is also sufficient to consider $0\leqslant\Theta_{23}<\pi/2$, if $P(r)^{(3)}_{e\to\mu}$ and $P(r)^{(3)}_{e\to\tau}$, respectively, are to be measured. In the case of matter-enhanced oscillations the situation is not as trivial, but using an analytical formula for the evolution of a neutrino state in matter as derived in [29] [Eq. (44) therein], one can also show that the evolution of an initial electron neutrino is

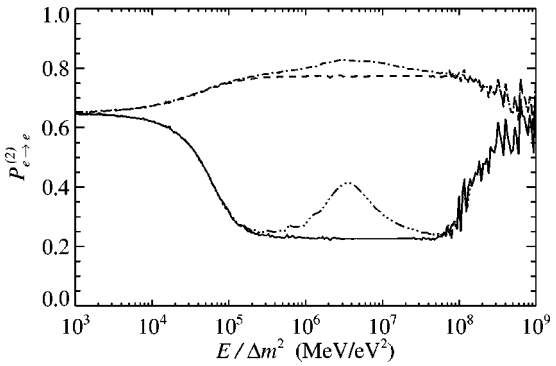

FIG. 1. Annually averaged probability of detecting a neutrino produced in the solar center as ν_e on Earth for $\sin^2 2\Theta = 0.7$ ($0 \leqslant \Theta < \pi/4$) with $\Delta m^2 > 0$ (solid and dash-dot-dot-dotted) and $\Delta m^2 < 0$ (dashed and dash-dotted line), respectively. The two lines in each case show the probability neglecting (solid and dashed) and including (dash-dot-dot-dotted and dash-dotted), respectively, the Earth-regeneration effect [34].

determined only by the squares of $\sin\Theta_{ij}$ and $\cos\Theta_{ij}$.

1. Two flavors

First, the case of two-flavor oscillations is examined. Exchanging the first and second rows in the definition of the mass eigenstates [Eq. (1)] implies that $\Delta m^2 \to -\Delta m^2$ and $\sin\Theta \leftrightarrow \cos\Theta [\Leftrightarrow \Theta \to (\pi/2 - \Theta)]$.[2] Since the assignment of the masses m_i to the respective mass eigenstate ν_j must not change the results, e.g., the case $\Delta m^2 > 0$, $0 \leqslant \Theta \leqslant \pi/4$ is equivalent to $\Delta m^2 < 0$, $\pi/4 \leqslant \Theta \leqslant \pi/2$ for any possible form of the Hamiltonian. Thus, without loss of generality Θ can be chosen to be within $[0, \pi/4]$.

For pure vacuum oscillations Eq. (10) can be applied which yields that $P(r)^{(2)}_{e\to e}$ is independent of the sign of Δm^2 *and* under the transformation $\Theta \to (\pi/2 - \Theta)$. Hence, in this case it is even sufficient to consider $\Delta m^2 > 0$.

The situation is different for oscillations in matter, where the resonance condition for the MSW transition is given by

$$N_{\rm res} = \frac{\Delta m^2/2E}{\sqrt{2} G_{\rm F}} \cos 2\Theta. \tag{11}$$

A resonance may occur if $N_{\rm res}$ is positive; thus, $\Delta m^2 > 0$ ($\Theta \leqslant \pi/4$). Although no resonance occurs for negative values of Δm^2, matter still influences the evolution of the neutrino flavor composition in the solar interior (for a more detailed study see, e.g., [28]).

In Fig. 1 the effect of solar matter on the energy dependence of $P^{(2)}_{e\to e}$ is demonstrated. For $E/|\Delta m^2| \lesssim 10^8$ MeV/eV^2 vacuum oscillations would yield an energy-independent survival probability for electron neutrinos, as the vacuum oscillation length is small and therefore only a mean value of [Eq. (10)]

[2]The indices 12 and 13 of the mass-squared difference and mixing angle, respectively, are omitted in the two-flavor case.

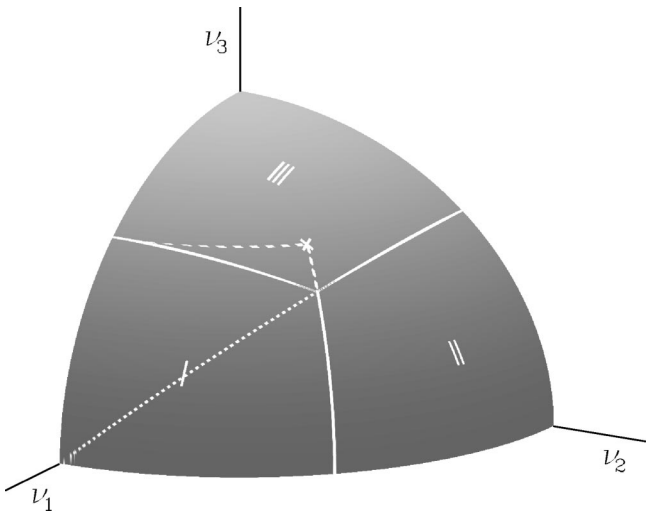

FIG. 2. Geometrical illustration of the flavor space available for a ν_e in the mass basis $(\nu_1, \nu_2, \nu_3)^T$. The spherical segment is divided into three sectors of equal size and shape, where each can be obtained from another by mirroring at the respective diagonal. Maximal mixing is given at the intersection of all three sector borders, i.e., $\sin^2 2\Theta_{12} = 1$ and $\sin^2 2\Theta_{13} = \frac{8}{9}$. The cross in sector III indicates the case $\sin^2 2\Theta_{12} = \sin^2 2\Theta_{13} = 1$; the dashed border extends sector I to the area with $\Theta_{12}, \Theta_{13} \leqslant \pi/4$. The dotted line splits sector I into two symmetric parts. (See text for more details.)

$$\langle P^{(2)}_{e\to e} \rangle_r = 1 - 0.5 \sin^2 2\Theta \tag{12}$$

would be measurable on Earth. For $\sin^2 2\Theta = 0.7$ this leads to $\langle P^{(2)}_{e\to e} \rangle_r = 0.65$. In contrast with the case with $\Delta m^2 > 0$ (solid line), where the resonant flavor conversion diminishes the ν_e contribution of the solar neutrino current, for $\Delta m^2 < 0$ (dashed line) the ν_e portion is even enhanced compared to the pure vacuum-oscillation case. Thus, the minimum value of the ν_e contribution for $\Delta m^2 < 0$ is obtained for pure vacuum oscillations. However, since vacuum oscillations in this mass range yield at most a suppression of the ν_e flux of 50% [Eq. (12)] and the solution to the solar neutrino problem demands, at least to explain the Homestake experiment, a stronger suppression of about 60%, for $\Delta m^2 < 0$ no reasonable solution can be obtained. Hence it is sufficient to consider in the two-flavor MSW case similar to the two-flavor vacuum oscillations solely $\Delta m^2 > 0 (\Theta \leqslant \pi/4)$.

Recently, it was pointed out in [32,35] that the 3σ ranges of the large mixing angle (LMA) and low mass-squared difference (LOW) solutions (see below) extend outside this region, but additional solutions for the solar neutrino problems could not be found there. In the analysis of [32] and [35], however, Δm^2 was fixed to be positive and thus $0 \leqslant \Theta < \pi/2$ has been examined. The part $\pi/4 < \Theta < \pi/2$ of that parameter space (termed the ''dark side'') is equivalent to the region $\Delta m^2 < 0$ and $0 < \Theta < \pi/4$ discussed above.

2. Three flavors

The considerations of the two-flavor case are now extended to three flavors. In Fig. 2 the flavor space for the electron neutrino is illustrated, where ν_e is represented as a

(yet unknown) point on the surface of an eighth of a unit sphere. While in the two-flavor case the ordering of the masses enables two cases to be distinguished ($\Delta m^2<0$ and $\Delta m^2>0$), in the three-flavor scenario six cases can be identified. But since exchanging any axes in Fig. 2 maps the flavor space onto itself, each mass hierarchy can of course be obtained from the ''canonical'' one ($m_1^2<m_2^2<m_3^2$) simply by exchanging the respective assignment of m_i to ν_j in Eq. (1).

Unlike the two-flavor case, where for pure vacuum oscillations the parameter space could be further decreased, this is not possible in the general three-flavor scenario, as, e.g., $\Delta m_{23}^2=\Delta m_{13}^2-\Delta m_{12}^2$ is not invariant under the transformation $\Delta m_{12}^2\rightarrow-\Delta m_{12}^2$.

For three-flavor neutrino oscillations in matter an exact analytic resonance condition can hardly be obtained because of the complicated formula for the mass eigenvalues ΔM_{ij}. If the masses are well separated, the two-flavor resonance condition [Eq. (11)] can be applied for both systems by substituting the quantities $(\Delta m^2, \cos 2\Theta)$ by $(\Delta m_{12}^2\cos\Theta_{13}, \cos 2\Theta_{12})$ and $(\Delta m_{13}^2, \cos 2\Theta_{13})$, respectively [36]. Hence, in this case considering $\Theta_{12},\Theta_{13}\leqslant\pi/4$ (sector I extended to the dashed borders in sector III of Fig. 2) with $\Delta m_{12}^2,\Delta m_{13}^2\geqslant 0$ is sufficient to obtain all possible solutions where two resonances may occur. However, the solution to the solar neutrino problem may also be a combination of a nonresonant and a resonant oscillation and the masses can be in principle very similar, too. Thus, the whole parameter space must be taken into account.

In [21], for instance, three-flavor oscillations were investigated assuming a canonical mass hierarchy and using a fixed value for $\Delta m_{13}^2=10^{-3}$ eV^2 in agreement with the atmospheric-neutrino results. They examined the remaining parameter space by applying an analytical formula for the ν_e survival probability, which approximates the solar electron-density profile by an exponential function and is valid for $\Delta m_{13}^2\approx 10^{-3}$ eV^2 and Δm_{12}^2 significantly smaller than Δm_{13}^2. Under these conditions the parameter space could be reduced considerably.

In the present work, the most general case of three-flavor oscillations of solar neutrinos is investigated, and thus these restrictions are not applicable here. Instead of performing a survey over the whole flavor space ($0\leqslant\Theta_{12},\Theta_{13}<\pi/2$) with canonical mass hierarchy, I prefer to consider the case $\Delta m_{12}^2,\Delta m_{13}^2>0$ which covers two possible mass hierarchies. Thus, in this case only half of the total flavor space must be overviewed. In the illustration provided in Fig. 2 this reduced area is given by sector II and the lower half of sector I defined by the dotted line.

To simplify the numerical survey and the analysis a variable transformation of the mixing angles is applied in each sector: Obviously $P_{e\rightarrow e}^{(3)}$ as defined in Eq. (9) is not symmetric under the exchange of indices $2\leftrightarrow 3$. However, sector I is symmetric under $\nu_2\leftrightarrow\nu_3$, and it would be useful to have two quantities $\tilde{\Theta}_{12}(\Theta_{12},\Theta_{13})$ and $\tilde{\Theta}_{13}(\Theta_{12},\Theta_{13})$ which satisfy

$$P_{e\rightarrow e}^{(3)}(\Delta m_{12}^2,\tilde{\Theta}_{12},\Delta m_{13}^2,\tilde{\Theta}_{13}) = P_{e\rightarrow e}^{(3)}(\Delta m_{13}^2,\tilde{\Theta}_{13},\Delta m_{12}^2,\tilde{\Theta}_{12}).$$

Defining in sector I ($0\leqslant\Theta_{12}<\pi/4$, $\tan\Theta_{13}\leqslant\cos\Theta_{12}$) the quantities $\tilde{s}_{12}(=\sin\tilde{\Theta}_{12})$ and $\tilde{s}_{13}$ by

$$\tilde{s}_{12}=s_{12},$$

$$\tilde{s}_{13}=\frac{s_{13}}{\sqrt{1-s_{12}^2c_{13}^2}}, \tag{13}$$

yields such a pair. With these quantities Eq. (9) is written as ($\tilde{c}_{ij}^2=1-\tilde{s}_{ij}^2$)

$$P(r)_{e\rightarrow e}^{(3)}=1-\left(\frac{2\tilde{c}_{12}\tilde{c}_{13}}{1-\tilde{s}_{12}^2\tilde{s}_{13}^2}\right)^2\left[\tilde{s}_{12}^2\tilde{c}_{13}^2\sin^2\left(\frac{\Delta m_{12}^2 r}{4E}\right)+\tilde{c}_{12}^2\tilde{s}_{13}^2\sin^2\left(\frac{\Delta m_{13}^2 r}{4E}\right)+\tilde{s}_{12}^2\tilde{s}_{13}^2\sin^2\left(\frac{\Delta m_{23}^2 r}{4E}\right)\right],$$

which is unaltered under exchange of the indices $2\leftrightarrow 3$.

Moreover, it can be proved that the evolution matrix of neutrinos in matter is not changed when exchanging the indices $2\leftrightarrow 3$ [9]. Hence, using $\tilde{s}_{12}$ and $\tilde{s}_{13}$ in sector I yields a ν_e survival probability, which is constant under this transformation in vacuum as well as in matter.

Similar to sector I also sector II ($\pi/4\leqslant\Theta_{12}<\pi/2$, $\tan\Theta_{13}\leqslant\sin\Theta_{12}$) can be brought into a quadratic shape by using the transformation

$$\tilde{s}_{13}=\frac{s_{13}}{\sqrt{1-c_{12}^2c_{13}^2}}. \tag{14}$$

But this does not yield a survival probability invariant under exchange of the indices $2\leftrightarrow 3$, as under this operation sector II would be mapped onto sector III.

III. CALCULATIONS

A. Standard solar model

For the following calculations my standard solar model (''GARSOM4'') as described in [37] is used. It has been calculated using the latest input physics, equation of state and opacity from the OPAL group [38,39], and nuclear reaction rates as proposed by [40]. In addition, microscopic diffusion of H, ^{3}He, ^{4}He, the CNO isotopes, and four heavier elements (among them Fe) is included using the diffusion constants of [41]. By treating convection as a fast diffusive process the chemical changes due to nuclear burning and diffusion (mixing) are evaluated in a common scheme.

A peculiarity of GARSOM4 is the inclusion of realistic 2D hydrodynamical model atmospheres [42] down to an optical depth of 1000. The improvement of the high-degree *p*-mode frequencies due to a better reproduction of the superadiabatic layers just below the photosphere is similar to the one obtained by using 1D-model atmospheres like in [3]. The advantage of using the 2D- instead of the 1D-model atmospheres is the extension of the former to greater optical depths, where the stratification is already adiabatic and thus

TABLE I. Typical quantities of GARSOM4. Here α_{CM} is the mixing-length parameter of the convection theory developed in [43]. Y and Z are helium and metal mass fractions, T and ρ the temperature and mass density, respectively. The depth of the convective envelope in units of the solar radius is abbreviated by R_{bce}. The indices i, s, and c denote initial, surface (photospheric), and central values, respectively.

α_{CM}	Y_i	Z_i	Y_s	Z_s	T_c (10^7 K)	ρ_c (g/cm^3)	R_{bce}	ρ_{bce} (g/cm^3)
0.975	0.275	0.020	0.245	0.018	1.57	152	0.713	0.188

the solar model becomes nearly independent of the applied convection theory.

In Table I typical quantities of GARSOM4 using the convection theory developed in [43] are summarized. The predicted event rates of GARSOM4 for the three presently operating types of neutrino experiments GALLEX/GNO/SAGE, Homestake, and Super-Kamiokande are summarized in Table II together with the values obtained by [4]. Since the input physics is very similar in both models, the predicted rates agree very well within the errors as quoted by [4]. In addition, the influence of the assumed ^{8}B-neutrino spectrum on the predicted rates is shown. Using the recent OG00 spectrum yields slightly higher rates for all three experiments than including the one of BL96, which is caused by the somewhat larger number of high-energetic ^{8}B neutrinos in the former spectrum and the strongly increasing detection probability toward higher energies.

Figure 3 shows the sound-speed profile of GARSOM4 compared to the seismic model inferred by [47]. The deviations of GARSOM4 from the latter are of the same size as standard solar models from other groups [4,48].

B. Neutrino-oscillation analysis

Using the neutrino flux as provided by GARSOM4 the evolution of the initial electron neutrinos through the Sun, space, and Earth is computed taking into account oscillations between the flavors (see the Appendix). The electron-density profile and the radial distribution of the neutrinos are taken from the solar model, too. For the electron-density profile of the Earth the spherically symmetric preliminary reference Earth model (PREM) [50] is applied. For each set of mixing parameters the neutrino energy spectrum observed on Earth is evaluated and folded with the detector response functions. The combinations of mixing parameters which reproduce the measured data are found by applying a χ^2 analysis.

There are four contributions to the total value of χ^2 originating from the four different available data sets: the event rates, the recoil-electron energy spectrum, the zenith-angle distribution, and the annual variation. The latter three are available only from the Super-Kamiokande detector, while to the first one all three types of neutrino experiments contribute.

For the event-rate portion the commonly used formula is

$$\chi^2_R = \sum_{i=1}^{3} \frac{(N_i^{\text{expt}} - N_i^{\text{th}})^2}{\sigma^2_{i,\text{expt}} + \sigma^2_{i,\text{th}}}, \tag{15}$$

where i denotes GALLEX/GNO/SAGE, Homestake or Super-Kamiokande. σ^2_{expt} and σ^2_{th} are the experimental and theoretical 1σ errors, respectively (Table II). Since the input physics in GARSOM4 is similar to the one used in [4], the theoretical errors derived therein are taken for σ^2_{th}. Here N_i^{expt} are the measured event rates, which are quoted together with the uncertainties in Table II. Note that the Super-Kamiokande data are usually reported as ^{8}B-neutrino flux relative to a standard solar-model prediction. Actually this

TABLE II. Expected event rates and neutrino flux, respectively, in the three types of experiments GALLEX/GNO/SAGE (Ga), Homestake (Cl), and Super-Kamiokande as predicted by the two solar models GARSOM4 and BP98 [4]. For GARSOM4 the expected values using the OG00 (first row) and the BL96 (second row) ^{8}B-neutrino spectrum are given. The last row provides the measured values with their respective errors.

	Ga [SNU]	Cl [SNU]	Super-K [10^6 cm^{-2} s^{-1}]
GARSOM4	128.7	7.79	5.18
	128.4	7.58	5.06
BP98	129^{+8}_{-6}	$7.7^{+1.2}_{-1.0}$	$5.15^{+1.00}_{-0.72}$
Experiment	74.2 ± 4.9 [a]	2.56 ± 0.23 [b]	2.40 ± 0.08 [c]

[a]Reference [44].
[b]Reference [45].
[c]Reference [46].

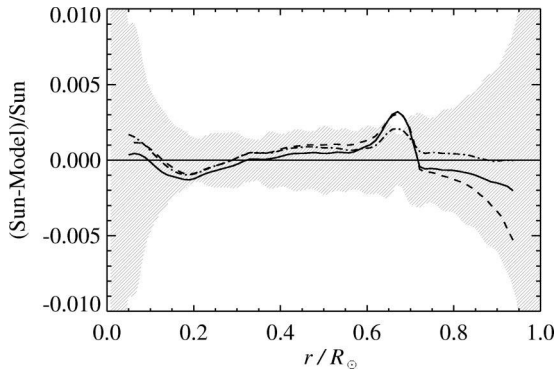

FIG. 3. Comparison of modern solar models with the seismic model by [47]: shown is the relative (seismic-solar model) difference of sound speed for the model of Ref. [4] (dashed line), Ref. [48] (dash-dotted line), and GARSOM4 (solid line). The grey-shaded area indicates a conservative error range of seismic models according to [49].

TABLE III. The χ^2 values in the case of no oscillations. χ^2(Ga), χ^2(Cl), and χ^2(SK) are the contributions of the GNO/GALLEX/SAGE, Homestake, and Super-Kamiokande experiments to χ^2_R [Eq. (15)]; χ^2_e, χ^2_Z, and χ^2_A are defined by Eq. (16).

χ^2(Ga)	χ^2(Cl)	χ^2(SK)	χ^2_e	χ^2_Z	χ^2_A	$\chi^2_{\rm tot}$
33.9	17.9	7.9	8.3	1.8	1.3	71.1

number has to be understood as an event-rate ratio. The total number of measured events is divided by the theoretically expected value (e.g., from GARSOM4). This ratio is then often falsely taken to be the suppression rate of the *total* ^{8}B-neutrino flux. However, with the energy window of the recoiled electrons being between[3] 5.5 and 20 MeV no statement about the total number of ^{8}B neutrinos below this window is possible. Moreover, neutrino oscillations may alter the energy spectrum of the ^{8}B-electron-neutrino flux, and as the scattering cross section of the neutrinos in Super-Kamiokande is energy dependent, the same number of event rates can be obtained with different ^{8}B-neutrino fluxes. Thus in the present analysis the event rate in Super-Kamiokande following Eq. (A5) is used and not the total ^{8}B-neutrino flux.

The recoil-electron energy spectrum is examined by

$$\chi^2_e = \sum_{i=1}^{18} \left(\frac{N^{\rm expt}_{i,e} - \alpha_e N^{\rm th}_{i,e}}{\sigma_{i,e}} \right)^2, \qquad (16)$$

where the sum extends over all 18 energy bins [Fig. 6(a)] and $\sigma_{i,e}$ is the quadratic sum of statistical and systematic errors taken from [46]. Since the absolute value of the event rate in Super-Kamiokande has already been used in χ^2_R the parameter α_e is introduced, by which the spectrum can be normalized adequately, independent of the total rates.

The contribution of the zenith-angle dependence [six bins, Fig. 6(b)] and seasonal-variation data [four bins, Fig. 6(c)] is defined analogously (denoted in the following χ^2_Z and χ^2_A, respectively).

In Table III the different χ^2 values for the no-oscillation case are provided. Taking into account the involved number of degrees of freedom ($N_{\rm DOF}$), these χ^2 values are in agreement with the values quoted in [24], where the energy spectrum and the day-night asymmetry are treated more elaborated. Obviously the event rate predicted for the gallium experiments differs most from the measured one, while as a result of the large uncertainty in the theoretical solar ^{8}B-neutrino flux, the Super-Kamiokande experiment provides the weakest significance for nonstandard neutrino properties. Nevertheless, it should be stressed that the strongest evidence for nonstandard neutrinos is obtained by the combined analysis of all three types of experiment [8].

[3]There are already data available for the energy window from 5.0 to 5.5 MeV, but the systematic errors are still to be derived.

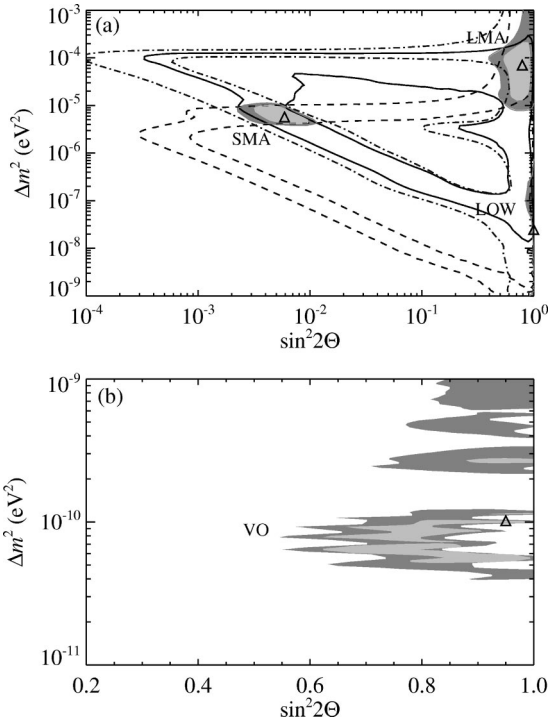

FIG. 4. Confidence regions in the Δm^2-sin^{2}2Θ plane for two-flavor neutrino oscillations using only the event rates. As a result of the different mass ranges and dependences on the mixing angle, the MSW solutions are shown in (a) and the pure vacuum-oscillation solutions in (b). The light shaded areas reflect the 95.4% C.L., while the dark shaded regions show the 99.7% C.L. Also drawn in (a) are the constraints from Homestake (solid line), GALLEX/GNO/SAGE (dashed line), and Super-Kamiokande (dash-dotted line). The best-fit value of each solution is indicated by △ (Table IV).

IV. RESULTS

A. Two flavors

In a first step the solar neutrino problem is analyzed taking into account oscillations only between two flavors. Figure 4 shows the allowed oscillation parameters using the OG00 ^{8}B-neutrino spectrum if solely the event rates of the

TABLE IV. Best-fit values for oscillations between two neutrinos taking into account solely the event rates of the three detector types. In the first four rows the OG00 ^{8}B-neutrino spectrum is included, while in the last rows the one of BL96 is assumed. The total number of DOF in this analysis is 1.

	Δm^2 (eV^2)	sin^{2}2Θ	$\chi^2_{\rm tot}$
SMA	5.7×10^{-6}	5.9×10^{-3}	0.16
LMA	7.1×10^{-5}	0.79	0.79
LOW	2.5×10^{-8}	1.00	5.00
VO	1.0×10^{-10}	0.95	0.16
SMA	5.4×10^{-6}	6.1×10^{-3}	0.21
LMA	7.3×10^{-5}	0.78	0.81
LOW	5.0×10^{-8}	1.00	3.70
VO	8.1×10^{-11}	0.73	0.61

TABLE V. Best-fit values for two-flavor neutrino oscillations and the respective χ^2 values taking into account all available data sets (event rates of GALLEX/GNO/SAGE, Homestake, and Super-Kamiokande and zenith-angle dependence, annual variation, and recoil-electron energy spectrum data of the latter). In the first four rows the recent OG00 ^{8}B-neutrino spectrum is utilized, while in the latter rows the BL96 spectrum is assumed. χ^2_R, χ^2_e, χ^2_Z, and χ^2_A are the individual contributions to $\chi^2_{\rm tot}$ as defined by Eqs. (15) and (16). The last row specifies the contribution of each χ^2 portion to $N_{\rm DOF}$ in this analysis is 26.

	Δm^2 (eV^2)	$\sin^2 2\Theta$	χ^2_R	χ^2_e	χ^2_Z	χ^2_A	$\chi^2_{\rm tot}/N_{\rm DOF}$
SMA	5.0×10^{-6}	3.7×10^{-3}	6.1	16.2	1.8	1.1	0.97
LMA	5.3×10^{-5}	0.79	0.9	8.6	2.0	1.2	0.48
LOW	1.1×10^{-7}	0.89	6.0	8.6	2.9	0.1	0.68
VO	6.9×10^{-10}	0.95	6.8	8.0	1.9	1.4	0.70
SMA	5.4×10^{-6}	4.2×10^{-3}	3.3	13.5	2.1	2.0	0.79
LMA	5.0×10^{-5}	0.88	2.0	10.9	1.8	1.7	0.63
LOW	1.0×10^{-7}	1.00	5.9	10.1	2.7	0.7	0.75
VO	8.6×10^{-10}	0.99	6.4	7.9	2.1	1.5	0.68
DOF			3	17	5	3	

three experiments are fitted. Clearly the four commonly known solution islands (see, e.g., [12,13]) can be identified, the small-mixing angle (SMA) and large-mixing angle (LMA), the low mass-squared difference (LOW), and the vacuum-oscillation (VO) solutions. The χ^2 values for the best-fit parameters in these solutions are quoted in Table IV. Apart from LOW all solutions have a ratio of χ^2 to $N_{\rm DOF}$ which is less than 1 and therefore these solutions are acceptable candidates as a correct solution for the solar neutrino puzzle.

In the last four columns in Table IV the best-fit values using the BL96 ^{8}B-neutrino spectrum are provided. The somewhat lower expected event rates (Table II) result in slightly different mixing parameters compared to the case using the recent OG00 spectrum (first four rows). While the χ^2 values for the SMA, LMA, and VO solutions are marginally worse with the BL96 spectrum, the LOW solution gives a slightly better fit to the experiments. However, the changes are in all cases relatively small.

Considering the event rates alone favors the SMA solution and, if the BL96 ^{8}B-neutrino spectrum is applied, the VO solution. However, the inclusion of the recoil-electron energy spectrum, the zenith-angle, and annual variations recorded by Super-Kamiokande into the analysis yields the LMA solution as the best fit (Table V). This behavior could also be found with the previous 825-day Super-Kamiokande data (e.g., in [51]). But in contrast to earlier analyses, where no parameter set could be deduced which would have reproduced all data sets at the same time [9], with the 1117-day data such simultaneous fits can be performed. In Table V the best-fit values of these solutions, the respective χ^2 contributions, and the ratio of $\chi^2_{\rm tot}$ to the available DOF are provided.

The 1σ, 2σ, and 3σ regions (63.7%, 95.4%, and 99.7% C.L.) including all available data (Fig. 5) are much bigger than in the case of taking solely the event rates (Fig. 4). The

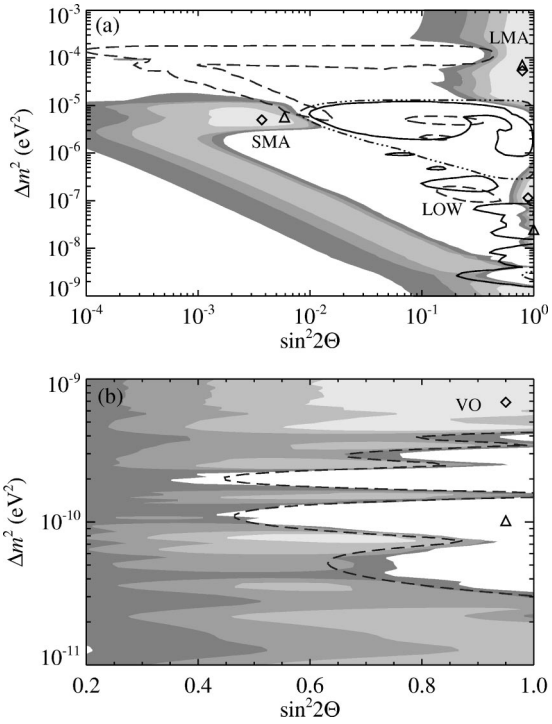

FIG. 5. Confidence regions in the Δm^2-$\sin^2 2\Theta$ plane for two-flavor neutrino oscillations using all data. The different shaded areas reflect from light to dark, 10%, 63.7%, 95.4%, and 99.7% C.L. Also drawn in (a) are the constraints from the recoil-electron energy spectrum (dashed line), zenith angle (dash-dotted line) and annual variation (solid line) of the Super-Kamiokande data. The best-fit value of this analysis is indicated by $\diamond$ (Table V); the $\triangle$ show the best-fit values of the analysis taking only the event-rate data (Table IV).

extension of the confidence regions of the SMA solution into the nonadiabatic regime at $\Delta m^2 < 10^{-6}$ eV^2 demands a more detailed explanation: With $N_{\rm DOF}$ in the analysis being 26, the 1σ confidence region is defined by $\chi^2_{\rm tot} - \chi^2_{\rm min} \lesssim 29$. As the minimal χ^2 value is about 12 ($=0.48\times26$, Table V), every set of parameters with $\chi^2_{\rm tot} \approx 41$ lies within the 1σ region. In the nonadiabatic regime of the SMA solution, the pep, ^{7}Be, ^{8}B, and CNO neutrinos are hardly influenced by MSW transitions. Thus, the predicted rates for Homestake and Super-Kamiokande are the no-oscillation ones, and the energy, zenith-angle, and annual spectra of the latter are expected to be constant. Since a constant ^{8}B-neutrino flux in Super-Kamiokande is in good agreement with the measurements (cf. Table III and Fig. 6) and the rates for the Ga detectors are excellently fitted within this region (see the dashed line in Fig. 4), the value for $\chi^2_{\rm tot}$ is about 37 which is certainly within the 1σ range.

In order to show that the most probable solution regions have indeed not changed drastically compared with the pure-rate analysis, the 10% C.L. areas are plotted in Fig. 5, too. The same region would result as the 1σ area if the minimum $\chi^2_{\rm tot}$ value would be zero instead of 12. Note that in some publications such as, e.g., [24], indeed not the ''true'' 1σ, 2σ, or 3σ ranges are provided, but instead, smaller χ^2 values have been chosen to yield the usual picture of three

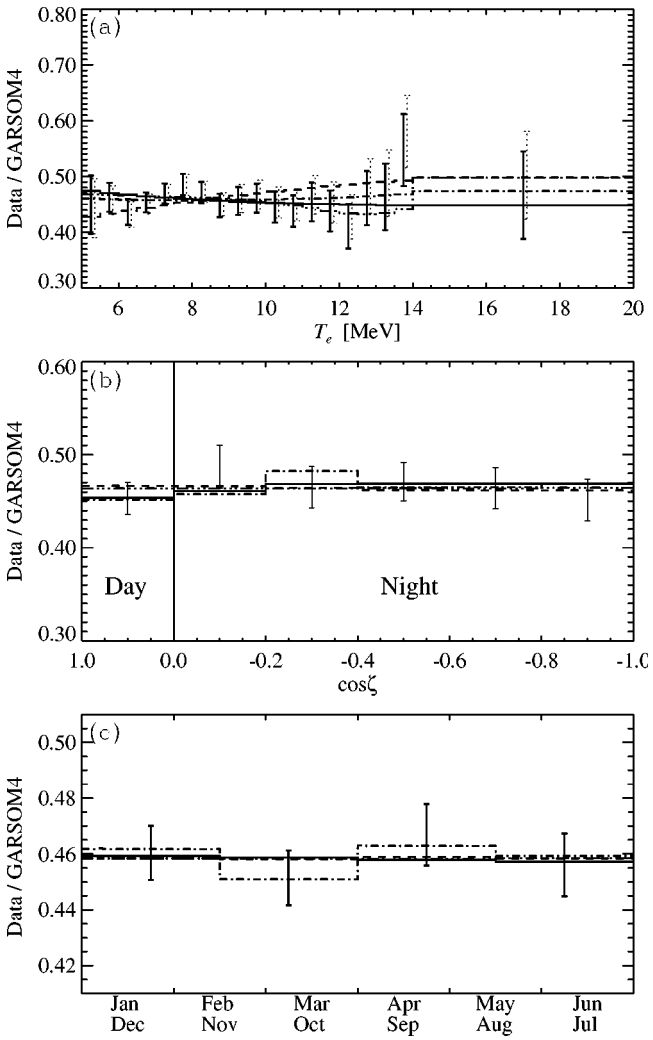

FIG. 6. Recoil-electron energy spectrum (a), zenith-angle (ζ) variation (b), and seasonal dependence of the best-fit LMA (solid line), SMA (dashed line), LOW (dash-dotted line), and VO (dash-dot-dot-dotted line) solutions in the two-flavor oscillation case including all available solar neutrino data (Table V, upper part) compared with the measurements of Super-Kamiokande (1117-day data [46]) using the OG00 (solid line) and BL96 ^{8}B-neutrino spectrum (dotted bins), respectively. All bins are equally spaced in the respective data area apart from the last bin in the energy spectrum, the range of which extends from 14 to 20 MeV. The flux variation due to the eccentric orbit of the Earth has been subtracted in (c).

MSW solution islands like in the pure-rate analysis.

Probably neglected correlations between the different data have caused the growth of the confidence regions. For instance, including the correlations between the rates of the three experiments can strongly change the values of χ^2_R, as has been shown, e.g., in [52]. Hence, for a more accurate analysis of the solar neutrino problem, all kinds of correlations should be included. For this purpose, more detailed data for the different spectra recorded by the Super-Kamiokande group are desirable. In addition, theoretical correlations between, e.g., the annual and zenith-angle data should be taken into consideration, too.

Independent of whether the BL96 or OG00 ^{8}B-neutrino spectrum is used, the LMA solution can reproduce each single kind of data, the event rates, the recoil-electron energy spectrum, the zenith angle, and the seasonal variation acceptably. Although $\chi^2_{\rm tot}/N_{\rm DOF}$ of the LOW and VO solutions are less than 1, these solutions do not lead to an acceptable fit of the event-rate data. Whether the SMA solution can already be ruled out by the new Super-Kamiokande data depends on the ^{8}B-neutrino spectrum included in the analysis. While with the BL96 spectrum the event rates can just be reproduced ($\chi^2_{\rm R}/N_{\rm DOF}\approx 1$), including the one of OG00 hardly yields a reasonable fit.

By assuming that the chlorine rate is due to unknown systematic errors 30% higher than quoted and by reducing the reaction rate for the ^{7}Be-proton capture by about 15–20 %, a VO solution could be obtained which would be able to reproduce the event rates *and* the energy spectrum of Super-Kamiokande fairly well [53]. However, presently there is no evidence for any hidden systematic uncertainties in Homestake, which would increase the event rate to the 3.5σ level.

The parameters of the best-fit LMA and SMA solutions are weakly modified when including all the data in the analysis (Tables IV and V). The recoil-electron energy spectrum mainly influences the SMA solution, while the zenith-angle data cause a slight shift of the best-fit values of the LMA solution (Fig. 5).

For $\Delta m^2\approx 10^{-7}$–$10^{-5}$ eV^2 the seasonal variations are caused by the zenith-angle variation (on the northern hemisphere more night data are recorded during winter than during summer), and thus no additional constraints can be obtained from the former data set in this parameter space. For smaller Δm^2 the eccentricity of the Earth's orbit leads to a ''real'' annual dependent signal, which can be used to constrain the mixing parameters. Note that in contrast to the $\Delta m^2\gtrsim 10^{-7}$ region the seasonal dependence in $\Delta m^2\lesssim 10^{-7}$ is now producing tiny day-night variations.

Anyway, for $\Delta m^2\lesssim 10^{-9}$ eV^2 deviations of less than 2% from an annually constant neutrino flux are predicted for the Super-Kamiokande data,[4] which is consistent within the errors with the recorded value. Thus, for the VO solutions only very weak constraints can be obtained from the present seasonal variation data, while for the region of the LOW solution these data provide important information. In fact, the position of the best-fit value of the LOW solution has been changed by including the annual-variation data in the analysis (Fig. 5).

In the regime of the VO solution, the recoil-electron energy spectrum provides very stringent constraints on the allowed mixing parameters, excluding a great part of the region favored by the rates. Hence, no good solution in the VO region could be found which reproduces the recoil-electron energy spectrum as well as the rates recorded in GALLEX/SAGE/GNO, Homestake, and Super-Kamiokande.

Therefore, the LMA solution is presently the favored solution to the solar neutrino problem, whereas the earlier fa-

[4]In the analysis of the seasonal data the neutrino signal has been corrected for the $1/r^2$ dependence of the flux.

vored SMA solution seems almost to be ruled out. But still, improved statistics in the recoil-electron data of Super-Kamiokande are required to identify more reliably the correct solution to the neutrino problem.

B. Three flavors

In spite of the fact that the two-flavor LMA solution is able to reproduce the recoil-electron energy spectrum, the zenith-angle and seasonal variations, and the event rates acceptably, the analysis is extended to all three families to deduce whether a better fit to the data can be achieved. Besides, this is the physically correct treatment, which contains the two-flavor case as a limiting one.

The electron-neutrino survival probability for three-flavor neutrino oscillations is determined by four quantities Δm^2_{12}, $\sin^2 2\Theta_{12}$, Δm^2_{13}, and $\sin^2 2\Theta_{13}$, where the appropriate pairs describe each the mixing of two flavors. Hence a four-dimensional parameter space has to be examined to deduce all possible solutions. In the Appendix the numerical realization is described with which the four-dimensional parameter survey can be performed efficiently. As worked out in Sec. II C, all possible solutions for MSW solutions are obtained by considering sectors I and II (Fig. 2) with Δm^2_{12}, $\Delta m^2_{13} > 0$. Using in sector I the quantity $\sin^2 2\tilde{\Theta}_{13}$ as defined in Eq. (13) instead of $\sin^2 2\Theta_{13}$ allows one to describe the pure two-neutrino ν_1-ν_3 oscillations equivalently to the ν_1-ν_2 case, which has been investigated thoroughly in various publications [12,13]. In addition, with the survival probability $P(r)^{(3)}_{e\to e}(\Delta m^2_{12}, \sin^2 2\Theta_{12}, \Delta m^2_{13}, \sin^2 2\tilde{\Theta}_{13})$ being symmetric in the exchange of the indices 2 and 3 unnecessary computations can be avoided. Nevertheless, the computations are very extensive due to the four-dimensional parameter space. Therefore, the grid in the three-flavor oscillation survey has to be chosen as less dense than in the two-flavor case, where only a two-dimensional grid had to be overviewed. However, the grid must still be fine enough that those solutions are not missed which might be confined to small regions in the parameter space. To balance the increased computational requirements the number of neutrino paths from the Sun to the detector to cover the whole year of data recording was reduced compared to the pure two-flavor neutrino oscillations. This leads to slightly different χ^2 values for effectively pure two-flavor solutions, which are also found in the full analysis.

Subspaces of the entire possible parameter space have been investigated, e.g., in [21] or [54]. In both publications an analytical expression for the survival probability $P^{(3)}_{e\to e}$ derived in [26] has been used, which is valid for large mass separations and small mixing angles, respectively. In this description $P^{(3)}_{e\to e}$ is determined by 2 two-flavor probabilities $P^{(2)}_{e\to e}$ for each mass splitting Δm^2_{12} and Δm^2_{13}. By approximating the electron-density profile in the solar interior with an exponential function, $P^{(2)}_{e\to e}$ can also be evaluated analytically [26].

The results obtained in [21] or [54] could always have been reproduced in the present work for the respective mass ranges. However, in those investigations of the three-flavor scenario, only the event-rate data were available. Using the new type of data (recoil-electron energy spectrum, zenith angle, and seasonal variations) almost all solutions found in [21,54] are disfavored. Furthermore, new solutions are identified since the respective parts of the parameter space were not covered in the analyses therein.

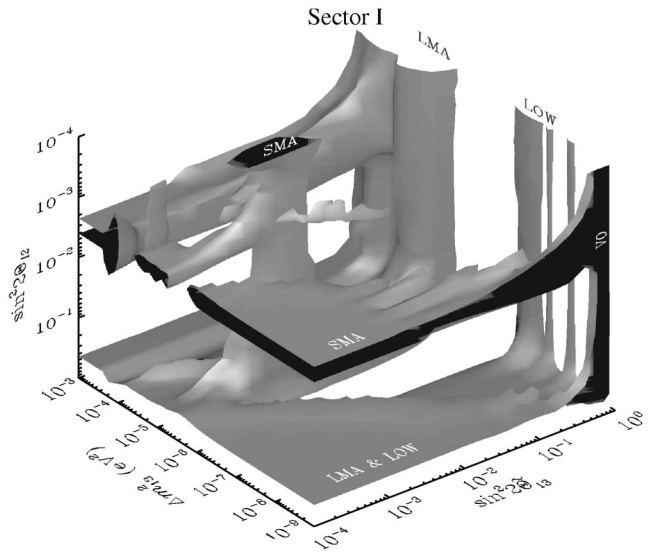

FIG. 7. Shaded volume representing the projection of the region with $\chi^2 \leq 26.5$ into the three-dimensional subspace of $\sin^2 2\Theta_{12}$-Δm^2_{13}-$\sin^2 2\tilde{\Theta}_{13}$ for MSW transitions in the $\nu_1 \leftrightarrow \nu_2$ and $\nu_1 \leftrightarrow \nu_3$ system (sector I). The allowed values are located within the light shaded surroundings. The position of the classical two-flavor solutions are also shown, which may be in the $1 \leftrightarrow 2$ as well as in the $1 \leftrightarrow 3$ system.

In the χ^2 analysis, applied to constrain the mixing parameters, always the whole available experimental data set was used for the present study. Furthermore, solely the OG00 ^{8}B-neutrino spectrum has been included. The Δm^2_{12}-Δm^2_{13} plane is divided according to the two-flavor case in three subregions where the two oscillation branches $\nu_1 \leftrightarrow \nu_2$ and $\nu_1 \leftrightarrow \nu_3$ are either both of matter type or both of vacuum type, or one of matter and the second of vacuum nature.

1. Oscillations in the MSW mass regime

First sector I is investigated, where $\nu_1 \leftrightarrow \nu_2$ and $\nu_1 \leftrightarrow \nu_3$ both may undergo a resonant MSW transition, i.e., $10^{-9} \leq \Delta m^2_{12}, \Delta m^2_{13} \leq 10^{-3}$ eV^2. In Fig. 7 the projection of the region with $\chi^2 \leq 26.5$ on the three-dimensional subspace $\sin^2 2\Theta_{12}$-Δm^2_{13}-$\sin^2 2\tilde{\Theta}_{13}$ is shown. The allowed parameters are located within the gray-shaded surroundings.

The pure two-flavor $\nu_1 \leftrightarrow \nu_3$ oscillations which are independent of the mixing into ν_2 recover in the vertical structures. For instance, the LMA and LOW solutions are represented by the half-pillars at $\sin^2 2\tilde{\Theta}_{13} = 1$ and $\Delta m^2_{13} \approx 5 \times 10^{-5}$ and 10^{-7} eV^2. The horizontal planes provide the solutions independent of ν_3, and thus are two-flavor oscillations in the $1 \leftrightarrow 2$ system, where the influence from Δm^2_{12} is not visible. However, the symmetry of sector I in the exchange of indices 2 and 3 implies that they must be equiva-

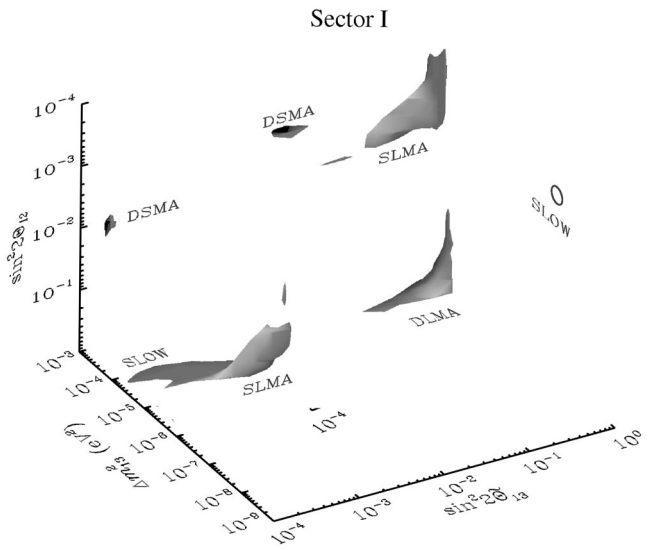

FIG. 8. Zoom into the shaded volume of Fig. 7 showing the position of the SLMA, DSMA, DLMA, and SLOW solutions. The shaded bodies enclose the regions with $\chi^2 \leqslant 15.4$. The circle in the $\sin^2 2\Theta_{12}$-Δm^2_{13} plane at $\sin^2 2\tilde{\Theta}_{13}=1$ shows the position of the tiny solution area of SLOW.

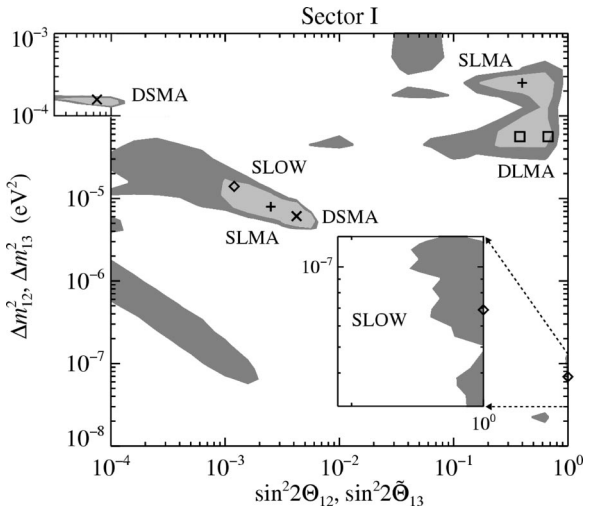

FIG. 9. Projection of the DSMA, DLMA, SLMA, and SLOW solutions onto the Δm^2_{12}-$\sin^2 2\Theta_{12}$ or the Δm^2_{13}-$\sin^2 2\tilde{\Theta}_{13}$ plane. The dark and bright shaded areas show the regions of $\chi^2 \leqslant 15.6$ and 13.9. Following the assignment of Table VI, the $\chi^2 \leqslant 13.9$ regions of the DSMA, SLMA, and SLOW solutions merge in the projection onto the Δm^2_{12}-$\sin^2 2\Theta_{12}$ plane, but are well separated in the Δm^2_{13}-$\sin^2 2\tilde{\Theta}_{13}$ plane (see also Fig. 8). The region with $\sin^2 2\tilde{\Theta}_{13} < 10^{-4}$ has been scanned separately only near the DSMA solution ($10^{-6} < \Delta m^2_{12} < 10^{-4}$ eV^2 and $10^{-4} < \sin^2 2\Theta_{12} < 10^{-2}$).

lent to solutions independent of ν_2. Therefore, the plane around $\sin^2 2\Theta_{12} \approx 1$ is equivalent to the pillarlike structures at $\sin^2 2\tilde{\Theta}_{13}=1$ and can thus be identified as an overlap of mainly LMA and LOW solutions. Similarly the plane at $\sin^2 2\Theta_{12} \approx 3 \times 10^{-3}$ represents the SMA solution. The three-flavor solutions with the smallest χ^2 values are sited near the intersection regions of the horizontal planes and vertical objects, which means that they are at least slightly more probable than the pure two-flavor solutions and involve indeed all three flavors.

In Fig. 8 the regions with $\chi^2 \leqslant 15.4$ of the present survey are shown. As a result of the symmetry in $\nu_2 \leftrightarrow \nu_3$ and the overlap of solution islands, in this projection the six basic regions in this figure belong only to four distinct solutions. Two of them can be identified as ''double'' SMA and LMA solutions, respectively, i.e., the same kind of solution in $\nu_1 \leftrightarrow \nu_2$ and $\nu_1 \leftrightarrow \nu_3$ (DSMA and DLMA, respectively). In addition, two solutions are combinations of a SMA solution in $\nu_1 \leftrightarrow \nu_2$ ($\sin^2 2\Theta_{12} \lesssim 10^{-3}$) and a LMA and LOW solution, respectively, in $\nu_1 \leftrightarrow \nu_3$ ($\sin^2 2\tilde{\Theta}_{13} \gtrsim 10^{-1}$ and $\Delta m^2_{13} \approx 10^{-4}$ and 10^{-7} eV^2, respectively), therefore denoted SLMA and SLOW. The extension of the SLOW solution in the $\sin^2 2\Theta_{12}$-Δm^2_{13} plane at $\sin^2 2\tilde{\Theta}_{13} \approx 1$ is very small and thus its position is marked by a small circle. The assignment of $\nu_1 \leftrightarrow \nu_2$ to SMA and $\nu_1 \leftrightarrow \nu_3$ to LMA and LOW, respectively, is ambiguous and could also be chosen vice versa. This is reflected by the second appearance of the SLOW and SLMA solutions in Fig. 8 at $\sin^2 2\Theta_{12} \gtrsim 10^{-1}$ and $\sin^2 2\tilde{\Theta}_{13} \lesssim 10^{-3}$. The respective solution islands merge in this projection.

In Fig. 9 the projection of the DSMA, DLMA, SLMA, and SLOW solutions into the typical two-flavor planes are shown. One of the areas labeled, for instance, SLMA has to be identified with oscillations in $\nu_1 \leftrightarrow \nu_2$ and the other with ν_1-ν_3 mixing. The oscillation parameters are provided in Table VI together with the χ^2 values. Since two more parameters are adjusted in the three-neutrino as compared to the two-neutrino case, N_{DOF} reduces from 26 to 24.

The mixing angle of the second small mixing-angle branch in the DSMA solution at $\sin^2 2\tilde{\Theta}_{13}$ is about two orders of magnitude smaller than the usual two-flavor SMA solution (compare Figs. 9 and 4). This second SMA branch causes an additional resonance at $E \approx 10$ MeV (see Fig. 10), which enables a better fit to the recoil-electron energy spectrum and the event rates (compare Tables V and VI). Thus a solution almost as good as the LMA solution could be obtained ($\chi^2_{\mathrm{tot}}/N_{\mathrm{DOF}}=0.5$).

The DLMA and SLMA solutions have almost the same values for χ^2_R, χ^2_e, χ^2_Z, and χ^2_A as the LMA solution (cf. Tables V and VI). Since no improvement in explaining the solar neutrino measurements could thus be achieved by combining the LMA solution with an additional oscillation in the $\nu_1 \leftrightarrow \nu_3$ system, the two-flavor LMA solution itself is a favored solution in the three-flavor analysis, too

In the SLOW solution the advantages of the two-flavor SMA and LOW solutions are united. While with the SMA solution the rates can be reproduced very well (see Table IV), the LOW solution provides good fits to the energy spectrum, the annual, and the zenith-angle variations (Table V).

The best-fit value of the SLOW solution for $\sin^2 2\tilde{\Theta}_{13}$ is equal to 1 and, thus, at the border of sector I to sector III. Exchanging the assignment of indices 2 and 3 transfers the SLOW solution to the border between sectors I and II. In the latter sector, where $\pi/4 \leqslant \sin\Theta_{12} \leqslant \pi/2$ and $\tan\Theta_{13} \leqslant \sin\Theta_{12}$, an additional survey has been performed, too.

TABLE VI. The most favored solutions within the three-flavor oscillation scenario and the respective χ^2 values. The second column indicates the sector in the flavor space, where the solution has been found (see also Fig. 2). Δm^2_{ij} is in units of eV^2 and s^2_{ij} abbreviates here $\sin^2 2\Theta_{ij}$. In sector I $\sin^2 2\tilde{\Theta}_{13}$ is defined by Eq. (13), analogously in sector II by Eq. (14). χ^2_R, χ^2_e, χ^2_Z and χ^2_A are the individual contributions to $\chi^2_{\rm tot}$ as defined by Eqs. (15) and (16). The number of DOF ($N_{\rm DOF}$) is 24.

		Δm^2_{12}	s^2_{12}	Δm^2_{13}	$\tilde{s}^2_{13}$	χ^2_R	χ^2_e	χ^2_Z	χ^2_A	$\chi^2_{\rm tot}/N_{\rm DOF}$
DSMA	I	6.1×10^{-6}	4.2×10^{-3}	1.6×10^{-5}	7.5×10^{-5}	0.6	8.2	1.9	1.2	0.50
DLMA	I	5.6×10^{-5}	0.67	5.6×10^{-5}	0.38	0.9	8.5	2.0	1.3	0.53
SLMA	I	7.9×10^{-6}	2.5×10^{-3}	2.5×10^{-4}	0.40	0.6	8.5	1.8	1.1	0.50
SLOW	I	1.4×10^{-5}	1.2×10^{-3}	6.9×10^{-8}	1.00	1.8	8.7	2.1	2.1	0.61
DVO	I	5.5×10^{-11}	0.64	2.9×10^{-10}	0.60	3.5	5.7	1.9	1.5	0.53
DVO′	II	1.2×10^{-10}	0.58	7.3×10^{-11}	0.79	2.3	6.8	1.9	1.5	0.52
SVO	I	2.7×10^{-10}	0.51	1.0×10^{-5}	2.5×10^{-3}	1.6	5.9	1.8	0.9	0.43
LVO	I	4.1×10^{-11}	0.70	1.7×10^{-4}	0.40	1.4	8.1	2.0	2.0	0.56
DOF						3	17	5	3	

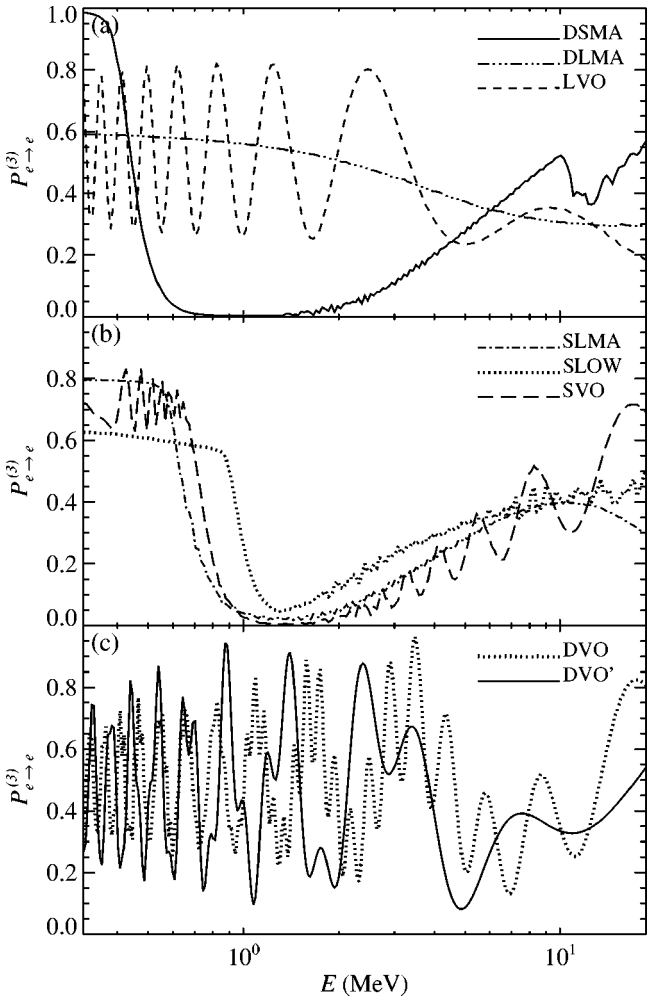

FIG. 10. The annually averaged survival probability of ^{8}B electron neutrinos detected on Earth for the deduced three-flavor solutions.

However, no new solutions could be identified; solely, the ''foothills'' of the SLOW solution into this sector have been found. Hence, in the mass regime with $10^{-9} \leqslant \Delta m^2_{12}, \Delta m^2_{13} \leqslant 10^{-3}$ eV^2 the region with $\pi/4 \leqslant \sin\Theta_{12} \leqslant \pi/2$ does not provide new solutions, which is similar to the findings in the two-flavor case, where neither any additional solution has been detected in this parameter range.

2. Three-flavor vacuum oscillations

In the case when both mass-squared differences are in the vacuum-oscillation regime ($\Delta m^2_{12}, \Delta m^2_{13} \leqslant 10^{-9}$ eV^2) two minima could be found, denoted DVO and DVO′. While DVO is located in sector I (Fig. 11), i.e., $0 \leqslant \Theta_{12} \leqslant \pi/4$, DVO′ has been found in sector II (Fig. 12), where $\pi/4 < \Theta_{12} \leqslant \pi/2$. Thus, although they seem to have very similar mixing parameters (Table VI), there are really distinct solutions with different properties (see Fig. 10). Note that while

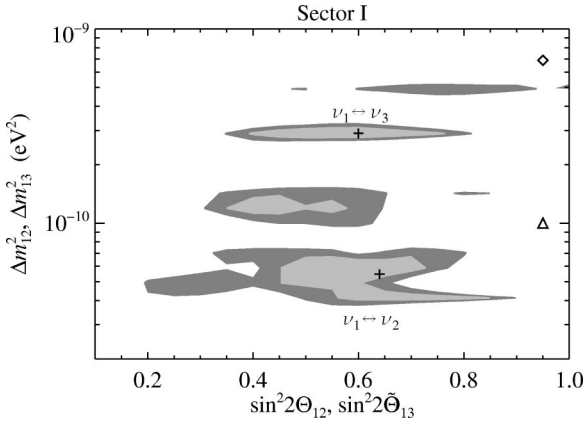

FIG. 11. Projection of the DVO solution onto the Δm^2_{12}-$\sin^2 2\Theta_{12}$ and Δm^2_{13}-$\sin^2 2\tilde{\Theta}_{13}$ plane, respectively. The χ^2 levels of the regions agree with those of Fig. 9 and the ''+'' symbols denote the best-fit values. The best-fit value of the two-flavor VO solution reproducing solely the event rates is marked by $\triangle$, while the position of the two-flavor VO solution in the complete analysis is shown by $\diamond$.

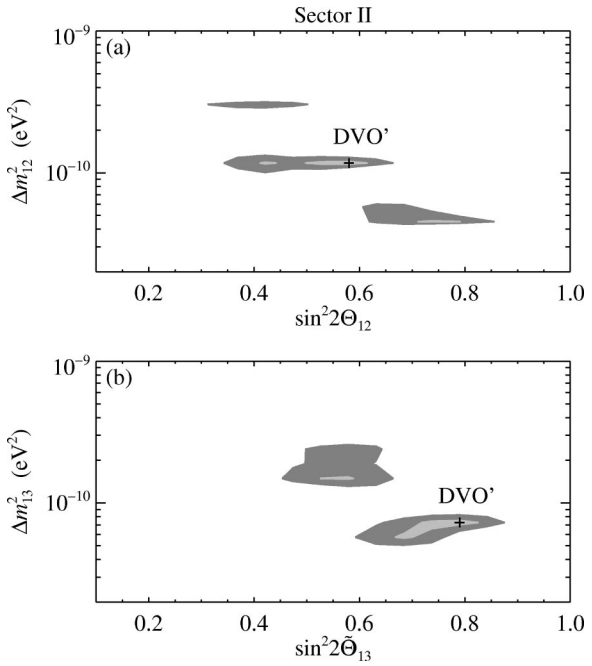

FIG. 12. Projection of the DVO′ solution onto the Δm^2_{12}-$\sin^2 2\Theta_{12}$ and Δm^2_{13}-$\sin^2 2\tilde{\Theta}_{13}$ plane. The χ^2 levels of the regions agree with those of Fig. 11.

in sector I the assignment of the indices can be exchanged, this is not possible in sector II. If an exchange of ν_2 and ν_3 in DVO′ is desired, the mixing angles have to be transformed appropriately to lie finally in sector III.

With the DVO and DVO′ solutions a slightly better fit to the recoil-electron energy spectrum can be achieved compared to the DSMA, DLMA, and SLMA solutions (Table VI and Fig. 13). However, because of the event rates being reproduced worse, the $\chi^2_{\rm tot}$ values of DVO and DVO′ are almost equal to the values of DSMA, DLMA, and SLMA.

Compared to the two-flavor VO solution an improved fit to the event rates has been obtained with the three-flavor vacuum-oscillation solutions, but still the event rates are fitted barely acceptably. The DVO and DVO′ solutions show a compromise between the VO solution ($\triangle$ in Fig. 11) obtained by fitting solely the event-rate data and the VO solution of the complete analysis ($\diamond$ in the same figure). The mixing angles for the three-flavor vacuum solution are only about one-half of the usual two-flavor VO solution, as ν_e is now oscillating nearly equally strong into *two* other flavors.

3. Mixed vacuum and MSW oscillations

The combination of oscillation between two neutrino flavors in the MSW mass regime and an additional vacuum oscillation into the third flavor is investigated, completing the mass ranges which have not been covered in the previous sections. This case has been examined in [54] for $10^{-7} \leqslant \Delta m^2_{13} \leqslant 10^{-4}$ eV^2 and $10^{-12} \leqslant \Delta m^2_{12} \leqslant 10^{-9}$ eV^2. However, in that analysis only the event rates have been included, but not the recoil-electron energy spectrum, the zenith-angle dependence, or the annual variation data recorded by Super-Kamiokande. Furthermore, the Earth-regeneration effect has been neglected. Therefore, this case is reinvestigated including all the available data and calculating the electron-neutrino survival probabilities fully consistently including the Earth effect like in the previous sections.

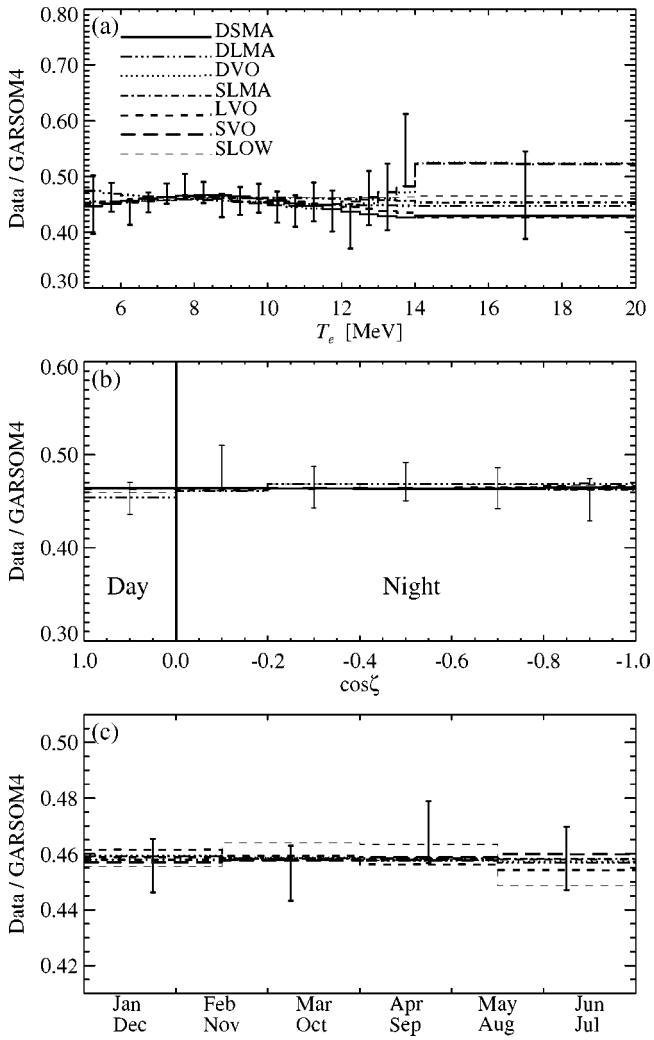

FIG. 13. Recoil-electron energy spectrum (a), zenith-angle (ζ) variation (b), and seasonal dependence (c) of the best-fit three-flavor solutions including all available solar neutrino data compared with the measurements of Super-Kamiokande. The experimental data agree with Fig. 6 using the OG00 ^{8}B-neutrino spectrum.

In this survey Δm^2_{13} is taken to be in the mass range of the MSW solutions ($10^{-9} \leqslant \Delta m^2_{13} \leqslant 10^{-3}$ eV^2) and Δm^2_{12} in the vacuum-oscillation area ($10^{-12} \leqslant \Delta m^2_{12} \leqslant 10^{-9}$ eV^2). With these conventions about Δm^2_{13}, two possibilities are conceivable for the $\nu_1 \leftrightarrow \nu_3$ system, a resonant and a nonresonant oscillation. Since the masses are well separated, the condition for a resonance obtained in the two-flavor case can be applied [Eq. (11)]:

$$N_{\rm res} = \frac{\Delta m^2_{13}/2E}{\sqrt{2} G_{\rm F}} \cos 2\Theta_{13} > 0.$$

Thus, an MSW flavor transition is only possible if the mixing angle Θ_{13} is less than $\pi/4$. In the $\nu_1 \leftrightarrow \nu_2$ system only pure

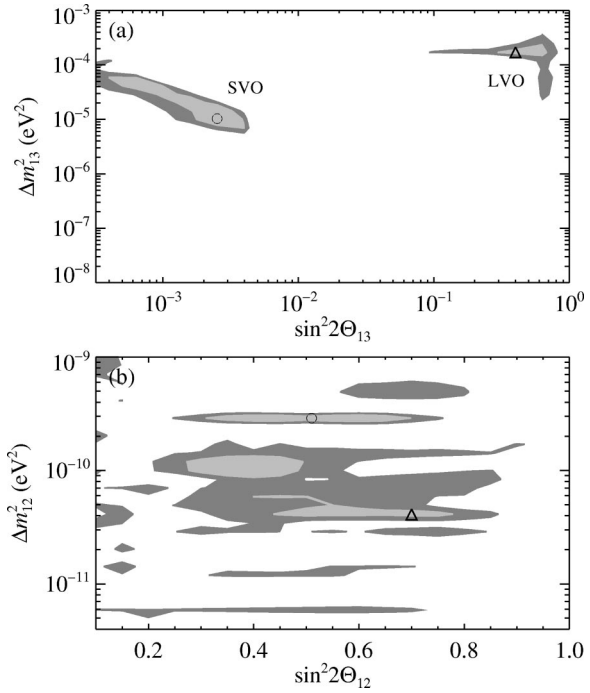

FIG. 14. Projections of the SVO and LVO solutions onto the Δm^2_{12}-$\sin^2 2\Theta_{12}$ and Δm^2_{13}-$\sin^2 2\Theta_{13}$ plane. The χ^2 levels are chosen to be 13.9 (bright) and 15.6 (dark shaded) like in the previous figures. The circles mark the best-fit values of the SVO solution, the triangles the one of the LVO solution ($\Theta_{12}, \Theta_{13} \leqslant \pi/4$).

vacuum oscillations occur, and thus $\Theta_{12} \leqslant \pi/4$. Since the solution may be a combination of a vacuum oscillation in the $1 \leftrightarrow 2$ and a resonant and nonresonant oscillation, respectively, in the $1 \leftrightarrow 3$ branch, the complete essential parameter space for $10^{-9} \leqslant \Delta m^2_{13} \leqslant 10^{-3}$ eV^2 and $10^{-12} \leqslant \Delta m^2_{12} \leqslant 10^{-9}$ eV^2 is therefore covered by $\Theta_{12} \leqslant \pi/4$ and $\Theta_{13} \leqslant \pi/2$.

Basically two minima could be found in the parameter space of this subsurvey, which are combinations of a SMA and a LMA solution, respectively, in $\nu_1 \leftrightarrow \nu_3$ ($\Theta_{13} \leqslant \pi/4$) and an additional VO mixing in $\nu_1 \leftrightarrow \nu_2$, therefore denoted SVO and LVO (Fig. 14). The SVO solution is similar to solution ''B'' found in [54]. Interestingly, the vicinity of the SVO solution has been explored intensively in [55], whereas the motivation was different: The mixing parameters of this solution agree with the neutrino properties predicted by a grand unification (GU) theory, where the neutrino masses are caused by the seesaw mechanism with the mass of the heaviest right-handed neutrino being of the order of the GU scale.

The fit of the LVO solution to the data is worse than the pure two-flavor LMA solution supporting the result of part 1 of this section: that the LMA solution cannot be improved on by including a third oscillation. However, the mass-squared difference of the LMA branch in the LVO as well as SLMA solution ($\Delta m^2_{13} \approx 2 \times 10^{-4}$ eV^2) is almost one order of magnitude higher than that of the LMA solution itself. The implication of this fact for the combined analysis of the solar and atmospheric neutrino problem will be discussed further in the final section.

The SVO solution is presently the favored solution to the solar neutrino problem, in contrast to all other three-flavor solutions even better than the two-flavor LMA solution. SVO combines the merit of the VO solution to explain the energy spectrum and the property of the SMA solution to reproduce the event rates (Table IV). Interestingly, this solution has also been found to be the best explanation of the solar neutrino problem, using the older 504- or 708-day data sets of Super-Kamiokande.

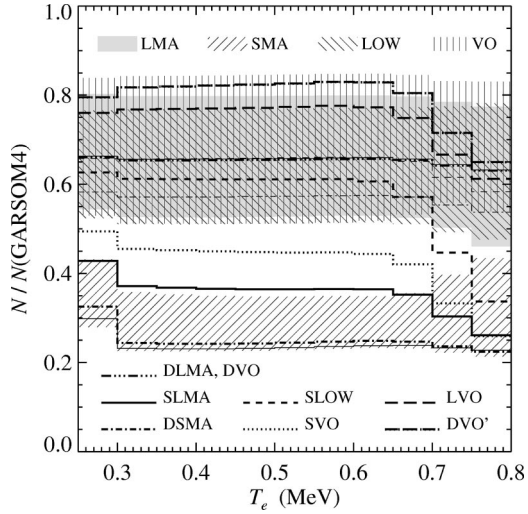

FIG. 15. Expected recoil-electron energy spectrum in Borexino for the best-fit two- and three-flavor solutions. The shaded and hatched areas have been obtained by allowing the mixing parameters to vary within the 10% region of the two-flavor LMA and SMA solutions, respectively, shown in Fig. 5. The thin lines represent the best-fit two-flavor solutions in the respective area (solid line, SMA and LMA, respectively, dash-dotted line, LOW; dashed line, VO).

V. PROSPECTS FOR FUTURE EXPERIMENTS

Future neutrino experiments like SNO or Borexino will provide further information to determine the correct solution to the solar neutrino problem. In the following the abilities of these detectors to discriminate the various two- and three-flavor solutions will be discussed.

A. Borexino

In Fig. 15 the expected recoil-electron energy spectrum in Borexino of the two- and three-flavor solutions is shown. The shades and hatched areas indicate the uncertainties in the mixing parameters of the 4 two-flavor solutions. These areas were obtained by allowing the mixing parameters to vary within the 10% confidence region of the Δm^2-$\sin^2 2\Theta$ plane (see Fig. 5).

While in the presently operating detectors the ^{7}Be neutrinos contribute, if at all, only a small portion to the total event rate, Borexino is going to measure basically these neutrinos (Fig. 16). In addition, the highest-energy bin of the recoil-electron spectrum ($T_e \geqslant 0.75$ MeV) is sensitive to the neutrinos of the CNO cycle and of the pep reaction. Borexino may also measure the high-energy part of the pp-neutrino spec-

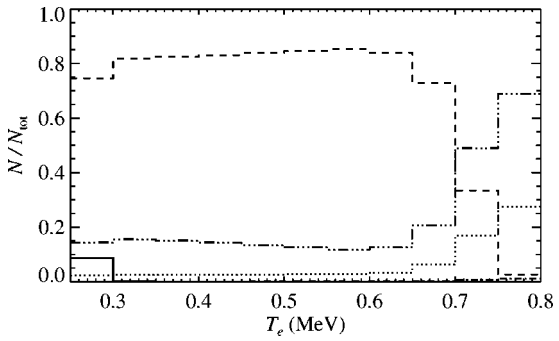

FIG. 16. The contribution of different neutrino types to the total event rate in Borexino in the case of no oscillations. The neutrino flux was derived from GARSOM4. The line styles correspond to *pp* (solid line), pep (dotted line), ^{7}Be (dashed line), CNO (dash-dot-dot-dotted line), and ^{8}B neutrinos (dash-dotted line).

trum, as these may contribute about 9% to the total rate in the lowest-energy bin ($T_e \leq 0.3$ MeV).

In the case of the SMA solution Borexino should detect only about 25% of the event rate as predicted by GARSOM4, while in the LMA case about 65% are expected (Fig. 15). Actually, for the SMA solution the rate is basically due to the interaction of the ν_μ (or ν_τ) with the detector, as in this solution the ^{7}Be neutrinos almost totally consist of ν_μ flavor. This leads to an unmistakable signal of the SMA compared to the LMA solution: an excess in the lowest-energy bin of about 30% compared to the other bins caused by the *pp* neutrinos. With the resonance in the SMA solution being at about 0.3 MeV, *pp* neutrinos do — unlike ^{7}Be or CNO neutrinos — not undergo an MSW transition. Thus, with good statistics in the low-energy bins SMA could be clearly distinguished from LMA.

One of the main advantages of this detector is the ability to monitor seasonal variations in the neutrino signal — the vacuum survival probability is modified by the eccentric orbit of the Earth [Eq. (10)]. Since the ^{7}Be neutrinos are in contrast to ^{8}B neutrinos emitted to 90% in a monoenergetic line at 0.862 MeV, the signal in the detector is not smeared out like in Super-Kamiokande. A detailed analysis about the sensitivity of Borexino to detect vacuum oscillations is given in [56].

The sensitivity of the ^{7}Be-neutrino flux in the VO regime is also visible in the zenith-angle dependence of the event rate in Borexino [thin solid line in Fig. 17(b)]. In particular, the rates of those zenith angles, under which the Sun appears only around the winter or summer solstice ($|\cos\zeta| \gtrsim 0.6$), are influenced by the modulation of the ^{7}Be-neutrino signal with the Sun-Earth distance. Note that unlike the Earth-regeneration effect, which in the MSW mass range can lead to a variation of the event rate with the zenith angle only during the night [see thin dashed line in Fig. 17(b) representing the LOW solution], for VO solutions a variation in the signal over the whole day is apparent. The magnitude of the zenith-angle variation, however, is smaller, as each zenith-angle bin is an average over many positions of the Earth in its solar orbit. Therefore, the seasonal variation of the event rates is more sensitive to detect VO solutions as the zenith-angle dependence. For the best-fit mixing parameters of the

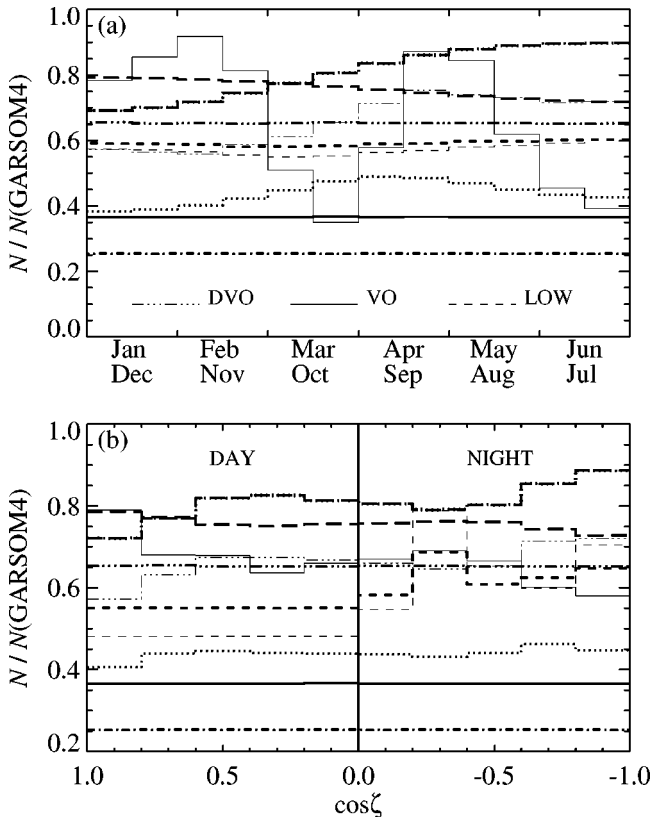

FIG. 17. Annual and zenith-angle variations of the recoil electrons in Borexino expected for the best-fit three-flavor solutions. The thick lines correspond to same solutions as in Fig. 15. In the seasonal variation (b) the flux changes due to the eccentricity of the Earth's orbit have been subtracted.

MSW solutions SMA and LMA no Earth regeneration takes place for the energy of the ^{7}Be neutrinos, and thus no zenith-angle variation of the event rates in Borexino is expected for these cases. In case of the LOW solution, however, day-night variations should be measured [thin dash line in Fig. 17(b)].

In summary for the two-flavor case, a total rate of about 30 ± 5 % compared to GARSOM4 is predicted for the SMA solution and about 65 ± 15 % for the LMA, LOW, and VO solutions. The latter three can be disentangled by using the zenith-angle and seasonal data. Great seasonal variations are expected for the VO solution, strong zenith-angle dependence during the night for LOW, and a constant neutrino flux during the whole year for the LMA solution, provided that the influence of the eccentric Earth orbit has been removed. Note that also for the SMA solution neither zenith-angle nor seasonal variations are expected.

The expected energy, zenith-angle, and seasonal dependences of the recoil electrons in Borexino for the best-fit values of the 8 three-flavor solutions are shown in Figs. 15 and 17, too. DSMA and DLMA cause signals very similar to their two-flavor counterparts SMA and LMA, respectively, and are therefore difficult to disentangle from the latter in any kind of the Borexino data.

But the SLOW solution leads to a clear signature in Borexino compared to the two-flavor solutions. It has a strongly reduced event rate of almost 50% in the high-energy bins of

Borexino, which are not observed in any other solution. The reason for this is the relatively high resonance energy of about 1 MeV (cf. Fig. 10), which causes a strong suppression of electron-type CNO and pep neutrinos, but a weaker reduction of ^{7}Be electron neutrinos. By way of contrast, the resonances of the SLMA and SVO solutions are about 0.8 MeV (Fig. 10), and thus, the ^{7}Be electron neutrinos are diminished more strongly than in the SLOW solution, which according to Fig. 16 yields smaller rates below 0.7 MeV.

In addition, the SLOW solution leads to a zenith-angle-dependent signal during the night due to the Earth-regeneration effect [Fig. 17(b)] caused by the LOW branch of this solution. Thus, a large day-night variation measured by Borexino would strongly favor LOW or SLOW. By additional data from the energy spectrum these solutions should then be distinguishable from each other.

The mean event rates expected for the SLMA and SVO solutions are within a region, where all other solutions are disfavored. Since for the SVO solution also annual variations are expected from its VO branch [see Fig. 17(a)], both solutions may be disentangled from each other and from all other solutions.

The properties of the pure three-flavor vacuum-oscillation solutions DVO and DVO′ are very sensitive to the exact mixing parameters. Even a very small variation in the mixing parameters of these solutions may produce a recoil-electron energy spectrum or seasonal changes which resembles that of the other or the LVO solution. Hence a discrimination between DVO, DVO′, and LVO will almost be impossible with Borexino.

These solutions are also difficult to distinguish from the two-flavor VO solution. However, the most probable value for Δm^2 of the VO solution is almost one order of magnitude larger than the VO branch(es) of DVO, DVO′, or LVO (compare Tables V and VI), yielding a more frequently varying annual signal for the VO solution. Hence, measuring a weak annually varying signal with only one maximum per half a year would at least provide a strong hint that the solution to the solar neutrino problem is rather a three-flavor DVO, DVO′, or LVO solution than a pure two-flavor VO solution.

B. SNO

Recently, SNO has started to measure solar neutrinos in the same energy window as Super-Kamiokande, however with a better energy resolution and the ability to discriminate the charged current (CC) and NC events. Since the total number of neutrinos does not change by neutrino oscillations (only their flavor), the number of NC events has to agree with the no-oscillation scenario; i.e., the total number of solar neutrinos independent of their flavor can be determined by this quantity.[5] Therefore, no departures in the recoil-electron energy spectrum, zenith angle, or seasonal dependence from the standard (no-oscillation) values are expected for NC events. The merit of SNO is the measurement of the ratio of CC to NC events, as with this quantity the ν_e contribution to the total solar neutrino flux is connected. A measured CC/NC ratio smaller than the standard one unambiguously proves that the solar neutrinos, initially ν_e's, are oscillating into another flavor during their flight from the solar interior to the Earth.

If the excess in the high-energy bins of Super-Kamiokande, which was apparent in the data published previously [14], reappears in the continuing measurements, the CC/NC ratio in SNO will enable one to discriminate between an explanation by neutrino oscillations and by an enhanced *hep* neutrino flux, which also was under discussion [51]. While for the latter solution the *hep*-neutrinos would contribute equally to the CC and NC events leading to a constant CC/NC ratio, for the oscillation scenario a similar excess like in Super-Kamiokande would be also apparent in the CC/NC ratio of SNO.

To illustrate the expectations for the recoil-electron energy spectrum and zenith-angle dependence of the CC events in SNO, the first and second moments of these distributions are calculated (for definition see [13]). The first moment provides the mean value and the second a measure of the width of the distribution.

With very small annual or daily changes in the Super-Kamiokande detector, such variations are neither expected for CC events (e-ν_e scattering) in SNO. Thus, for the zenith-angle moments in SNO only small deviations from the standard value are predicted for the two-flavor SMA, LMA, LOW, and VO solutions [Fig. 18(b)]. The largest deviations of about 4% may be measured in case of the LMA solution being correct.

The error bars for these solutions in Fig. 18 were obtained in the same manner as for the recoil-electron energy spectrum in Borexino. Since the best-fit values are not very well separated and also the error bars strongly overlap in the plane of the first two zenith-angle moments, it seems to be very difficult to disentangle the two-flavor solution by forthcoming zenith-angle data of SNO. A similar behavior is expected for the moments of the recoil-electron energy spectrum [57] shown in Fig. 18(a). However, since the energy resolution in SNO is better than in Super-Kamiokande (Table VII), more significant data can be expected to disentangle the true solution to the solar neutrino problem. A more detailed discussion about the properties of SNO to discriminate the two-flavor solutions can be found in [58].

In the energy moments a large area is still allowed for the VO solution. In case Borexino does not record any seasonal variations all solutions containing a VO branch (e.g., LVO) and, in particular, the two-flavor VO solution would hardly be correct. Deviation of $< -5\%$ in the second energy moment would then favor the DSMA solution.

Nevertheless, from Fig. 18 it becomes obvious that, only if SNO is measuring a big deviation of the energy or zenith-angle moment from the standard (no-oscillation) value, one of these solution can be favored, as, e.g., $\gtrsim 3\%$ in the first zenith angle further supports LMA as correct solution to the solar neutrino problem. But since SNO may well detect no such deviations, we need additional results from Borexino to exclude some of the presently possible solutions.

[5]Provided no mixing with sterile neutrinos occurs.

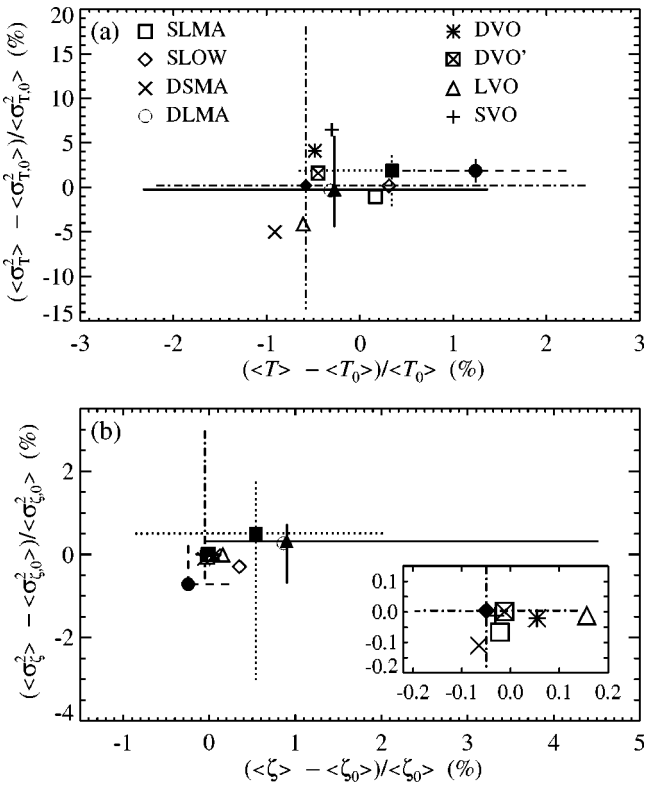

FIG. 18. Predicted values for the moments of the recoil-electron energy (upper panel) and zenith-angle spectrum (lower panel) for CC events in SNO in case of the three-flavor solutions. The solid symbols represent the two-flavor solutions LMA (▲), SMA (●), LOW (■), and VO (♦) of Fig. 4. The error bars were obtained in the same manner as the hatched and shaded areas, respectively, in Fig. 15.

VI. DISCUSSION

The most favored solutions to the solar neutrino problem in the scope of two- and three-flavor neutrino oscillations have been investigated in this work. For this purpose the evolution of the neutrino state was followed numerically from the solar interior, where the neutrinos are produced in the fusion reactions, through the Sun, space, and Earth to the neutrino detectors without falling back to analytical approximations (cf. the Appendix).

Eight solutions in the three-flavor case could be found, where the SVO solution has already been detected previously, e.g., by [54] and [55] neglecting the Earth-regeneration effect. The SVO, SLMA, and DSMA are at least as probable as the presently favored two-flavor LMA solution. The DVO, DVO′, LVO, DLMA, and SLOW solutions, with which the measured event rates, recoil-electron energy spectrum, zenith-angle dependence, and annual variation are reproduced slightly worse than with the other 3 three-flavor solutions, are nevertheless still good candidates as solutions to the solar neutrino problem. The new experiments Borexino, which will soon start to operate, and SNO, which is already taking data, and improved statistics in Super-Kamiokande possibly will enable one to discriminate the various two- and three-flavor solutions. Basically, with Borexino the vacuum-oscillation solutions will leave a clear footprint in the annual variation of the event rates, with which they can be distinguished from MSW solutions. Additionally, in the case of the SLOW solutions the high-energy bins of the recoil-electron energy spectrum will be significantly depleted compared to the other energy bins and a day-night asymmetry of about 10% is expected, which only can be reproduced by the two-flavor LOW solution.

TABLE VII. Energy resolution parameters used in the present work. The values for Super-Kamiokande and SNO are taken from [57]. For Borexino Δ_1 the energy resolution width at 1 MeV provided by L. Oberauer (private communication) is quoted.

	Super-K	SNO	Borexino
Δ_{10}	1.6 MeV	1.1 MeV	47 keV
δ	10 keV	100 keV	—

In this work it was investigated whether the two-flavor solutions of the solar neutrino problem can be improved by including all three flavors. But the three-flavor case cannot be examined totally independent of the results obtained for the atmospheric neutrinos. The most promising solution to the atmospheric neutrino problem is presently the oscillation between ν_μ and ν_τ with the mass-squared difference Δm_{23}^2 being approximately 10^{-3} eV^2 [59,24]. This demands that the sum or difference of Δm_{12}^2 and Δm_{13}^2 of the three-flavor solutions for the solar neutrino problem be about 10^{-3} eV^2. However, none of the presented three-flavor solutions satisfies this condition, which implies that either three-flavor solutions are excluded favoring the two-flavor LMA solution ($\Theta_{13}=0$) or that the origin of the atmospheric neutrino problem is not ν_μ-ν_τ oscillations.

Analyzing the atmospheric neutrino deficit using three-flavor neutrino oscillations it has been found in [60] that with $\Delta m_{23}^2 \approx 10^{-4}$ eV^2 solutions exist if Δm_{12}^2 and $\sin^2 2\Theta_{12}$ are in the vicinity of the SMA solution and $4° \lesssim \Theta_{13} \lesssim 22°$ [Fig. 2(d) in [60]]. Indeed, the SLMA solution satisfies this condition as its SMA branch ($\nu_1 \leftrightarrow \nu_2$) is close to the two-flavor SMA solution and the best-fit parameters of the LMA branch are $\Delta m_{13}^2 = 2.5\times 10^{-4}$ and $\Theta_{13}=19°$ (cf. Table VI). However, with the improved atmospheric neutrino data of Super-Kamiokande, the solutions with $\Delta m_{23}^2 \lesssim 10^{-3}$ eV^2 are almost ruled out (see, e.g., [24]), strongly disfavoring the SLMA solution. Analogously the LVO solution, the LMA branch of which ($\nu_1 \leftrightarrow \nu_3$) has similar parameters as the SLMA solution (Table VI), is inconsistent with the atmospheric neutrino data.

A further possible solution to the atmospheric neutrino problem may be the oscillation into a sterile neutrino, which is neglected in this work. So it cannot be excluded that three-flavor oscillation solutions with a sterile and an active neutrino branch exist, which solve both the solar and atmospheric neutrino problems.

In the two-flavor solutions LMA, SMA, LOW, and VO it is implicitly assumed that mixing into the third flavor is negligible. Thus, these solutions are not coupled to the atmospheric neutrino problem, as they can easily be taken as ν_e-ν_μ oscillations, where no mixing between ν_e and ν_τ ap-

pears. If, however, the results of the LSND Collaboration [61], which claimed to have detected ν_e-ν_μ oscillations with $\Delta m^2_{12} \gtrsim 10^{-2}$ eV^2, are confirmed by the MiniBooNE experiment [62], it will be difficult to solve the solar and atmospheric neutrino anomaly simultaneously by the oscillation of three neutrino flavors. A four-neutrino scheme has been proposed (one sterile and three active neutrinos) to cover the three different mass scales involved by the LSND result, atmospheric and solar neutrino problems (see, e.g., [63]). In any case, identifying the solution to the solar neutrino puzzle by the future data of forthcoming and presently operating solar neutrino detectors may also constrain solutions for the atmospheric neutrino problem or vice versa.

The possibility that two-flavor neutrino oscillations are responsible for the solar neutrino puzzle appears to be supported by the relatively weak improvement of the fit by increasing the parameter space from two (two flavors) to four dimensions (three flavors). Indeed, only with the SVO solution a somewhat better fit to the data could be achieved compared to the LMA solution. This can be taken as a hint that the errors in the data of Super-Kamiokande are greater then assumed, perhaps still unknown systematic errors exist, or that the statistics is still insufficient. Moreover, correlations between the different data sets of Super-Kamiokande probably are important for a more accurate and reliable analysis of the solar neutrino data.

Anyway, if the explanation of the atmospheric neutrino deficit is, despite the presently strong evidence, found not to be neutrino oscillations, three-flavor oscillations are allowed in any mass range, implying that the SVO solution leads to the best fit to the data. Remarkably, SVO has been found to be the favored solution also when taking the previous 504- or 708-day data sets of Super-Kamiokande [9]. Hence, SVO is together with the two-flavor LMA solution one of the stablest explanations for the solar neutrino problem.

ACKNOWLEDGMENTS

I am grateful to Achim Weiss and Wolfgang Hillebrandt for their inspiring comments and suggestions. Furthermore, the support of Georg Raffelt in particle-physics questions is acknowledged. I also want to thank Jørgen Christensen-Dalsgaard for his help in further improving the solar model. Moreover, I am thankful to Sarbani Basu for providing me the seismic model, to Scilla Degl'Innocenti for the seismic error data, to John N. Bahcall for the detector response functions and other useful quantities of SNO, and to Lothar Oberauer for the data about the Borexino properties. This work was supported by the ''Sonderforschungsbereich 375-95 für Astroteilchenphysik'' der Deutschen Forschungsgemeinschaft.

APPENDIX: FROM THE INITIAL NEUTRINO STATE TO THE EVENT RATES

To obtain event rates for the various detectors a variety of averages and integrals have to be evaluated. In this section briefly a numerical scheme is described as to how accurate predictions for the event rates can be calculated numerically.

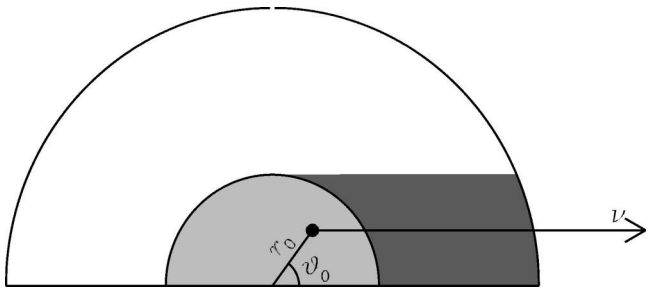

FIG. 19. Illustrating the definition of r_0 and ϑ_0. The light shaded region reflects the region of neutrino production; the dark shaded is covered by about 50 different ray paths (see text) with direction to the Earth (arrow labeled ν).

For a certain set of parameters Δm^2_{12}, Δm^2_{13}, $\sin^2 2\Theta_{12}$, and $\sin^2 2\Theta_{13}$ the evolution of an initially pure electron neutrino from the solar interior to the terrestrial detectors has to be evaluated. Therefore,

$$|\nu_i(r)\rangle = e^{-i\tilde{H}r}|\nu_i^e\rangle \tag{A1}$$

must be integrated [cf. Eq. (5)]. Here $|\nu_i^e\rangle$ denotes the initial electron-neutrino state given by Eq. (8). The evolution starts at a point inside the Sun given by r_0 and ϑ_0 (see Fig. 19). The neutrino path has then to be followed through the Sun, space, and, if necessary, Earth arriving at the detector at day D under zenith angle ζ. From the final state $|\nu_i^{\mathrm{f}}\rangle$ the electron-neutrino survival probability $P_{e\to e}(\Delta m^2_{12}/E, \Delta m^2_{13}/E, \sin^2 2\Theta_{12}, \sin^2 2\Theta_{13}, r_0, \vartheta_0, D, \zeta)$ is derived using the relation

$$P_{e\to e} = |\langle \nu_i^{\mathrm{f}}|\nu_i^e\rangle|^2. \tag{A2}$$

Since none of the detectors are able to discriminate between ν_μ and ν_τ, the contribution of these neutrino families is simply given by $1 - P_{e\to e}$.

First, the neutrino paths through the Sun are considered. Since N_e—and thus also the Hamiltonian $\tilde{\mathcal{H}}$—is a function of r, the integration of Eq. (A1) is performed piecewise. For this purpose, the interior of a solar model is subdivided into a grid equally spaced in electron density (about 500 grid points). By approximating the electron density between two neighboring grid points linearly, Eq. (A1) can be solved analytically. Thereby the neutrino state can be followed through the whole solar interior. Furthermore, the accuracy is improved by increasing the grid density near the resonance [Eq. (11)].

Most of the neutrinos emerge between $0 < r_0 \lesssim 0.4 R_\odot$ and $0 \leqslant \vartheta_0 \leqslant \pi$. If the MSW resonance lies within this region, it is crucial to carefully calculate the paths for neutrinos with different r_0, as the more centrally produced neutrinos may undergo a MSW conversion, while the outermost are hardly influenced by the matter. Paths with $\vartheta_0 > \pi/2$ may cross the MSW-resonance region even twice. The contribution of a neutrino emerging at an angle ϑ_0 and radius r_0 to the total flux originating in this shell is given by

$$\Omega(\vartheta_0) = 0.5 \sin(2\vartheta_0) \mathrm{d}\vartheta_0$$

for $0 \leqslant \vartheta_0 \leqslant \pi/2$. From the symmetry around the plane $\vartheta_0 = \pi/2$ it follows that $\Omega(\vartheta_0) = \Omega(\pi - \vartheta_0)$.

Since all neutrinos cross the shell $0.4R_\odot \lesssim r_0 \leqslant R_\odot$, a set of paths through this area is established (generally about 50, equally spaced in $\sin\vartheta_0$) on which $\exp(-i\tilde{\mathcal{H}}r)$ is calculated numerically by adding up the solutions in each region linearized in N_e. Thus, a set of matrices is obtained, $\mathcal{S}_\odot(\sin\vartheta_0)$, which describes the evolution from $r \approx 0.4R_\odot$ to the solar surface. By this means the neutrino state $|\nu_i^\odot(r_0,\vartheta_0)\rangle$ is evaluated by first integrating Eq. (A1) until $r \approx 0.4R_\odot$ and then using that matrix $\mathcal{S}_\odot(\sin\vartheta_0)$, which was calculated for a path closest to the actual path of $|\nu_i(r_0,\vartheta_0)\rangle$. It turns out that calculating solely two paths ($\vartheta_0 = 0$ and π) yields in most cases already acceptable results. Then, of course, only one matrix $S_\odot(0)$ is needed.

Now, the state $|\nu_i^\odot(r_0,\vartheta_0)\rangle$ is followed until the surface of the Earth using the equation for the vacuum oscillations [Eq. (6)]. Since the Earth orbit is eccentric, different days D during a year are discriminated (about 20 from perihelion to aphelion). In a final step the rotation of the Earth and thus the different paths of a neutrino through the Earth's interior during 1 day are considered. Here a procedure similar to the shell outside the fusion region of the Sun is applied: A set of about 30 matrices $\mathcal{S}_E(\sin\zeta)$ is calculated integrating $\exp(-i\tilde{\mathcal{H}}r)$ through the Earth.

By applying finally Eq. (A2) the survival probability $P_{e\to e}(r_0,\vartheta_0,D,\zeta)$ for a certain set of parameters $\Delta m_{12}^2/E$, $\Delta m_{13}^2/E$, $\sin^2 2\Theta_{12}$, $\sin^2 2\Theta_{13}$ is obtained. This is the basic quantity from which the final event rates are calculated.

Since the experiments provide data binned in certain periods (e.g., day, night, annual seasons, or a whole year) and in certain ranges of the zenith angle, respectively, $P_{e\to e}(r_0,\vartheta_0,D,h)$ first has to be integrated using the zenith-angle weights $W_\lambda(\zeta,D)$ (see, e.g., [13]) for each period D at the detector latitude λ.

After that, $P_\lambda^k(r_0,\vartheta_0)$ is folded with the radial distribution $\Phi_r(r_0)$ of the neutrino sources inside the Sun and the angle weights Ω discriminating the different neutrino types (pp, ^{7}Be, ^{8}B, etc., denoted by the superscript f). The event rates in the detectors are obtained by finally folding P_λ^f with the energy spectrum of each neutrino type Φ_E^f and the detector response function $\Xi_i(E)$, and summing up the contribution of all neutrino types. This yields

$$N_i = \sum_f \int P_\lambda^f \Xi_i(E')\Phi_E^f(E')\mathrm{d}E', \tag{A3}$$

where i is either Ga or Cl. The detector response function for the Homestake detector can be found, e.g., in [18] and for the Ga detectors in [64].

In Super-Kamiokande, Borexino, and SNO the energy spectrum of the recoil electrons can be measured at least within certain energy bins. Furthermore, SNO is able to discriminate CC and NC events, while Super-Kamiokande and Borexino measure the total number of events arisen by any neutrino flavor. According to [57] the response function for these type of experiments with recoil-electron energy between T_0 and T_1 can be described by

$$\Xi_\Upsilon(E,T_0,T_1) = \int_{T_0}^{T_1}\mathrm{d}T \int \mathrm{d}T' R(T,T')\frac{\mathrm{d}\sigma_\Upsilon(E,T')}{\mathrm{d}T'}, \tag{A4}$$

where with

$$R(T,T') = \frac{1}{\sqrt{2\pi}\Delta_{T'}}\exp\left(-\frac{(T'-T+\delta)^2}{2\Delta_{T'}^2}\right)$$

the energy resolution of the detector is included. Therein δ accounts for a possible uncertainty in the absolute energy calibration and Δ_T is the energy resolution width following the photon statistics which yields

$$\Delta_T = \Delta_{10}\sqrt{\frac{T}{10\ \mathrm{MeV}}},$$

with Δ_{10} being the energy resolution at 10 MeV. The parameters Δ_{10} and δ for Super-Kamiokande, SNO, and Borexino are summarized in Table VII.

The cross sections $\mathrm{d}\sigma_\Upsilon(E,T)/\mathrm{d}T$ for Super-Kamiokande and Borexino were calculated following the description in [65]. Υ denotes either ν_e and ν_μ (or equivalently ν_τ) for the interaction of these neutrino flavors with Super-Kamiokande and Borexino or CC and NC, respectively, for the reaction type in the SNO detector. With $\Xi_\Upsilon(E,T_0,T_1)$ given by Eq. (A4) the event rates in Borexino and Super-Kamiokande, respectively, are obtained from

$$N_i^k(T_0,T_1) = \sum_f \int [(1-P_\lambda^{k,f})\Xi_{\nu_\mu}(E',T_0,T_1) + P_\lambda^{k,f}\Xi_{\nu_e}(E',T_0,T_1)]\Phi_E^f(E')\mathrm{d}E', \tag{A5}$$

while the number of CC and NC events in SNO is defined analogously to the gallium and chlorine detector [Eq. (A3)]. With the threshold energy being greater than 5 MeV only the sum over ^{8}B and *hep* neutrinos has to be performed in Super-Kamiokande and SNO.

[1] R. Davis, Jr., D. S. Harmer, and K. C. Hoffman, Phys. Rev. Lett. **20**, 1205 (1968).

[2] W. A. Dziembowski, P. R. Goode, A. A. Pamyatnykh, and R. Sienkiewicz, Astrophys. J. **445**, 509 (1994); S. Basu *et al.*, *ibid.* **460**, 1064 (1996); H. M. Antia, Astron. Astrophys. **307**, 609 (1996); S. Basu, M. H. Pinsonneault, and J. N. Bahcall, Astrophys. J. **529**, 1084 (2000).

[3] H. Schlattl, A. Weiss, and H.-G. Ludwig, Astron. Astrophys. **322**, 646 (1997).

[4] J. N. Bahcall, S. Basu, and M. H. Pinsonneault, Phys. Lett. B **433**, 1 (1998).

[5] M. Gabriel, Astron. Astrophys. **309**, 939 (1996); O. Richard, S. Vauclair, C. Charbonnel, and W. A. Dziembowski, *ibid.* **312**, 1000 (1996).

[6] GALLEX Collaboration, P. Anselmann *et al.*, Phys. Lett. B **285**, 376 (1992). The GALLEX Collaboration measured solar

neutrinos from May 1991 to January 1998 interrupted by some maintenance work and calibration experiments. In July 1998 the facilities were taken over by the newly formed GNO group (Gallium Neutrino Observatory). After an extension of the gallium target to 60 t and further technical improvements the detector has been taking data again since the spring of 1999.
[7] SAGE Collaboration, J. N. Abdurashitov *et al.*, Phys. Lett. B **328**, 234 (1994).
[8] N. Hata and P. Langacker, Phys. Rev. D **52**, 420 (1995).
[9] H. Schlattl, Ph.D. thesis, Technical University Munich, 1999.
[10] B. Pontecorvo, Zh. Éksp. Teor. Fiz. **53**, 1717 (1967) [Sov. Phys. JETP **26**, 984 (1968)].
[11] S. P. Mikheyev and A. Yu. Smirnov, Yad. Fiz. **42**, 1441 (1985) [Sov. J. Nucl. Phys. **42**, 913 (1985)]; L. Wolfenstein, Phys. Rev. D **17**, 2369 (1978).
[12] N. Hata and P. Langacker, Phys. Rev. D **56**, 6107 (1997); H. Schlattl, A. Bonanno, and L. Paternò, *ibid.* **60**, 113002 (1999); J. N. Bahcall, P. I. Krastev, and A. Yu. Smirnov, Phys. Lett. B **477**, 401 (2000).
[13] J. N. Bahcall and P. I. Krastev, Phys. Rev. C **56**, 2839 (1997).
[14] Super-Kamiokande Collaboration, Y. Fukuda *et al.*, Phys. Rev. Lett. **82**, 2430 (1999).
[15] Super-Kamiokande Collaboration, Y. Fukuda *et al.*, Phys. Rev. Lett. **82**, 1810 (1999).
[16] J. N. Bahcall, P. I. Krastev, and A. Yu. Smirnov, Phys. Rev. D **58**, 096016 (1998).
[17] C. E. Ortiz *et al.*, Phys. Rev. Lett. **85**, 2909 (2000).
[18] J. N. Bahcall *et al.*, Phys. Rev. C **54**, 411 (1996).
[19] L.E. Marucci *et al.*, Phys. Rev. Lett. **84**, 5959 (2000); Phys. Rev. C **63**, 015801 (2001).
[20] R. Schiavilla *et al.*, Phys. Rev. C **58**, 1263 (1998).
[21] G. L. Fogli, E. Lisi, and D. Montanino, Phys. Rev. D **54**, 2048 (1996).
[22] T. Teshima, T. Sakai, and O. Inagaki, Int. J. Mod. Phys. A **14**, 1953 (1999); J. S. Kim and C. W. Kim, hep-ph/9909428.
[23] G. L. Fogli, E. Lisi, D. Montanino, and A. Palazzo, Phys. Rev. D **62**, 013002 (2000).
[24] M. C. Gonzalez-Garcia, M. Maltoni, C. Peña-Garay, and J. W. F. Valle, Phys. Rev. D **63**, 033005 (2001).
[25] G. G. Raffelt, *Stars as Laboratories for Fundamental Physics* (University of Chicago Press, Chicago, 1996).
[26] S. T. Petcov, Phys. Lett. B **214**, 259 (1988).
[27] K. Dick, M. Freund, M. Lindner, and A. Romanino, Nucl. Phys. **A562**, 29 (1999).
[28] V. Barger, K. Whisnant, S. Pakvasa, and R. J. N. Philips, Phys. Rev. D **22**, 2718 (1980).
[29] T. Ohlsson and H. Snellman, J. Math. Phys. **41**, 2768 (2000).
[30] J. Lundell and H. Snellman, Phys. Lett. B **470**, 163 (1999).
[31] A. Friedland, Phys. Rev. Lett. **85**, 936 (2000).
[32] A. de Gouvêa, A. Friedland, and H. Murayama, Phys. Lett. B **490**, 125 (2000).
[33] Particle Data Group, C. Caso *et al.*, Eur. Phys. J. C **3**, 1 (1998).
[34] J. Bouchez *et al.*, Z. Phys. C **32**, 499 (1986); S. P. Mikheyev and A. Yu. Smirnov, in *Proceedings of the 7th Moriond Workshop on New and Exotic Phenomena*, edited by O. Fackler and T. T. Vân (Frontières, Paris, 1987), p. 405; M. Spiro and D. Vignaud, Phys. Lett. B **242**, 279 (1990).
[35] M. C. Gonzalez-Garcia and C. Peña-Garay, Phys. Rev. D **62**, 031301 (2000).
[36] T. K. Kuo and J. Pantaleone, Phys. Rev. Lett. **57**, 1805 (1986).
[37] H. Schlattl and A. Weiss, Astron. Astrophys. **347**, 272 (1999).
[38] F. J. Rogers, F. J. Swenson, and C. A. Iglesias, Astrophys. J. **456**, 902 (1996).
[39] C. A. Iglesias and F. J. Rogers, Astrophys. J. **464**, 943 (1996).
[40] E. G. Adelberger *et al.*, Rev. Mod. Phys. **70**, 1265 (1998).
[41] A. A. Thoul, J. N. Bahcall, and A. Loeb, Astrophys. J. **421**, 828 (1994).
[42] B. Freytag, H.-G. Ludwig, and M. Steffen, Astron. Astrophys. **313**, 497 (1996).
[43] M. Canuto and I. Mazzitelli, Astrophys. J. **370**, 295 (1991); **389**, 724 (1992).
[44] GALLEX Collaboration, W. Hampel *et al.*, Phys. Lett. B **447**, 127 (1999); GNO Collaboration, M. Altmann *et al.*, *ibid.* **490**, 16 (2000); SAGE Collaboration, J. N. Abdurashitov *et al.*, Phys. Rev. C **60**, 055801 (1999); G. Gavrin for the SAGE Collaboration, talk given at the XIX International Conference on Neutrino Physics and Astrophysics, Sudbury, Canada, 2000.
[45] B. T. Cleveland *et al.*, Astrophys. J. **496**, 505 (1998).
[46] Y. Suzuki, talk given at the XIX International Conference on Neutrino Physics and Astrophysics, Sudbury, Canada, 2000.
[47] S. Basu, Mon. Not. R. Astron. Soc. **298**, 719 (1998).
[48] J. Christensen-Dalsgaard *et al.*, Science **272**, 1286 (1996).
[49] S. Degl'Innocenti, S. Dziembowski, W. A. Fiorentini, and B. Ricci, Astropart. Phys. **7**, 77 (1997).
[50] A. M. Dziemonski and D. L. Anderson, Phys. Earth Planet. Inter. **25**, 207 (1981).
[51] J. N. Bahcall, P. I. Krastev, and A. Yu. Smirnov, Phys. Rev. D **60**, 093001 (1999).
[52] G. L. Fogli and E. Lisi, Astropart. Phys. **3**, 185 (1994).
[53] V. Berezinsky, G. Fiorentini, and M. Lissia, Astropart. Phys. **12**, 299 (2000).
[54] Q. Y. Liu and S. T. Petcov, Phys. Rev. D **56**, 7392 (1997).
[55] K. S. Babu, Q. Y. Liu, and A. Yu. Smirnov, Phys. Rev. D **57**, 5825 (1998).
[56] A. de Gouvêa, A. Friedland, and H. Murayama, Phys. Rev. D **60**, 093011 (1999).
[57] J. N. Bahcall, P. I. Krastev, and E. Lisi, Phys. Rev. C **55**, 494 (1997).
[58] J. N. Bahcall, P. I. Krastev, and A. Yu. Smirnov, Phys. Rev. D **62**, 093004 (2000).
[59] Super-Kamiokande Collaboration, Y. Fukuda *et al.*, Phys. Rev. Lett. **82**, 2644 (1999).
[60] T. Sakai and T. Teshima, Prog. Theor. Phys. **102**, 629 (1999).
[61] LSND Collaboration, C. Athanassopoulos *et al.*, Phys. Rev. C **58**, 2489 (1998).
[62] MiniBooNE Collaboration, A. O. Bazarko, Nucl. Phys. B (Proc. Suppl.) **91**, 210 (2001).
[63] G.L. Fogli, E. Lisi, and A. Marrone, Phys. Rev. D **63**, 053008 (2001).
[64] J. N. Bahcall, Phys. Rev. C **56**, 3391 (1997).
[65] J. N. Bahcall, M. Kamionkowski, and A. Sirlin, Phys. Rev. D **51**, 6146 (1995).